

# Interventional Assays for the Latent Space of Autoencoders

Felix Leeb<sup>\*†</sup>Stefan Bauer<sup>‡†</sup>Bernhard Schölkopf<sup>‡</sup>

## Abstract

The encoders and decoders of autoencoders effectively project the input onto learned manifolds in the latent space and data space respectively. We propose a framework, called latent responses, for probing the learned data manifold using interventions in the latent space. Using this framework, we investigate "holes" in the representation to quantitatively ascertain to what extent the latent space of a trained VAE is consistent with the chosen prior. Furthermore, we use the identified structure to improve interpolation between latent vectors. We evaluate how our analyses improve the quality of the generated samples using the VAE on a variety of benchmark datasets.

## 1 Introduction

Autoencoders (AEs) [1, 2] and its modern variants like the widely used variational autoencoders (VAEs) [3], are a powerful paradigm for self-supervised learning for generative modeling [4], compression [5], anomaly detection [6] or natural language processing [7]. The popularity of autoencoders across various application domains comes from their ability to efficiently and effectively learn a transformation to and from the data distribution through a low dimensional latent space without requiring labeled data.

This makes autoencoders particularly useful for computer vision tasks where samples can be very high dimensional making processing, transmitting, and search prohibitively expensive. For images VAEs in particular have shown intriguing performance not just for generative modeling where they can outperform autoregressive baselines [8] and obtain state-of-the-art results for image density estimation [9].

The learned latent space should contain meaningful lower-dimensional representations of our world [10] and facilitate efficient downstream learning [11, 12], exhibit better generalization [13, 14] and increased interpretability as well as allow for causal reasoning [15]. While representation learning approaches based on autoencoders are thus already deployed across many disciplines and applications as well as an open research topic, real-world generative distributions can form inherently complicated manifolds in high dimensional spaces, making modeling and sampling challenging [16, 17].

Not capturing (or correctly interpolating on) the manifold can in turn lead to catastrophic results, e.g., when applied to fair decision making [18, 19] or medical imaging [20, 21]. Given the widespread adoption and use of autoencoded representation learning even in safety critical areas, the goal of this work is to provide and offer tools for an in depth understanding of the learned representation of VAEs.

We summarize our contributions as follows:

<sup>\*</sup>Email: fleeb@tuebingen.mpg.de

<sup>†</sup>Max Planck Institute for Intelligent Systems, Tübingen, Germany

<sup>‡</sup>Department of Electrical Engineering and Information Technology at ETH, Zürich, Switzerland

- We develop a framework, called *latent responses*, which identifies what parts of the latent space contain information and which latent dimensions share information.
- Using *latent responses*, we define the *structure score* to measure the extent to which the aggregate posterior deviates from the unstructured prior to make the representation more expressive and complex.
- We develop tools to analyze the manifold of the representation in the latent space for meaningful interpolation between samples.
- When true labels are available, we use the *conditioned latent responses* to identify where in the representation information for each true factor of variation is encoded and introduce the *Causal Disentanglement Score* to quantify how disentangled the representation is when taking the decoder into account.

## 2 Background

For a detailed discussion about autoencoders (sec. A.1) and latent manifolds (sec. A.3) we refer to the supplemental material A, and presently discuss only variational autoencoders in more detail since they are the focus of this work.

**Variational Autoencoders** (VAEs) [22, 23] are a framework for optimizing a latent variable model  $p_\theta(\mathbf{x}) = \int_{\mathbf{z}} p_\theta(\mathbf{x} | \mathbf{z}) p(\mathbf{z}) d\mathbf{z}$  with parameters  $\theta$ , typically with a fixed prior  $p(\mathbf{z}) = \mathcal{N}(\mathbf{z}; \mathbf{0}, \mathbf{I})$ , using amortized stochastic variational inference. A variational distribution  $q_\phi(\mathbf{z} | \mathbf{x})$  with parameters  $\phi$  approximates the intractable posterior  $p_\theta(\mathbf{z} | \mathbf{x})$ . The approximate posterior and generative model, typically called encoder and decoder and parameterized by neural networks, are jointly optimized by maximizing the ELBO (Evidence Lower BOund) which is a lower bound to the log likelihood:

$$\log p_\theta(\mathbf{x}) \geq \mathbb{E}_{q_\phi(\mathbf{z} | \mathbf{x})} [\log p_\theta(\mathbf{x} | \mathbf{z})] - D_{\text{KL}}(q_\phi(\mathbf{z} | \mathbf{x}) \| p(\mathbf{z})) = \mathcal{L}_{\theta, \phi}^{\text{ELBO}}(\mathbf{x}). \quad (1)$$

In  $\beta$ -VAEs, the KL term is modulated by a factor  $\beta$  to enforce a more structured latent space [24, 25].

It is common to regularize the objective to encourage certain structure in the latent space. The most popular kind of regularization encourages the latent manifold to resemble a specific known prior distribution to enable generating new observations by decoding samples from the prior.

This statistical formulation of VAEs may be unified with the functional view of autoencoders (with  $h_\phi^{\text{enc}} : \mathbb{R}^D \mapsto \mathcal{Z}$  and decoder  $h_\theta^{\text{dec}} : \mathbb{R}^d \mapsto \hat{\mathcal{X}}$ ) by recognizing that the aggregate posterior  $q_\phi(\mathbf{z}) = \int q_\phi(\mathbf{z} | \mathbf{x}) \pi(\mathbf{x}) d\mathbf{x}$  defines the distribution over  $\mathcal{Z}$  where  $\pi(\mathbf{x}) = \frac{1}{N} \sum_i^N \delta(\mathbf{x}_i - \mathbf{x})$  is the empirical true generative process from the  $N$  samples  $\mathbf{x}_i$  we observe). Similarly, the learned generative process  $p_\theta(\hat{\mathbf{x}}) = \int p_\theta(\hat{\mathbf{x}} | \mathbf{z}) p(\mathbf{z}) d\mathbf{z}$  is the distribution over  $\hat{\mathcal{X}}$ . It thus becomes apparent that the first term in the ELBO corresponds to the objective to match the decoder output to the observations, while the second term serves as regularization of the encoder output to match the chosen prior, thereby enabling variational inference and generation. For a more detailed discussion and related work about matching the prior distribution we refer to section A.2 in the appendix A.

## 3 Related Work

**Analysis and Understanding of Autoencoders.** Linear autoencoders [1] have been investigated early on [26, 27] in particular with a focus on the connection to principal component analysis (PCA) [28]. For variational autoencoders there has been significant work on understanding alternative formulations, which do not rely on the variational Bayes formulation [29], focus on disentanglement [25], robustness properties [30], the approximation quality [31], over-pruning [32], or again the connections to principal component analysis (PCA) [33, 34]. VAEs have additionally been investigated from an information theoretic viewpoint [35, 36] and with respect to training problems like posterior collapse [37] or the holes problem [38]. More recently there has been a focus on generalization [39] and memorization abilities of autoencoders [40, 41].

**Evaluating representations.** In generative modeling, representations are typically evaluated by log likelihood, ELBO, or perceptual metrics such as FID [42], IS [43], or precision/recall [44, 45]. Compression capability can also be evaluated e.g. in the context of bits-back coding, where it is formally related to the ELBO [46, 5, 47]. In general, representation quality has also been measured

in terms of disentanglement [48–52], robustness [53], or the complexity of learning downstream predictors [54]. However, while multiple metrics have been proposed, they are typically not agreeing and additional perspectives are needed [55].

## 4 Latent Responses

The latent response framework we develop here aims to take advantage of the surprisingly robust projection abilities of autoencoders to directly probe the learned data manifold in the latent space. More specifically, we start by applying an intervention in the latent space, decode, and then re-encode the generated point (equation 2) to quantify the effect of the intervention in the latent space. As long as the intervention does not take us too far away from the learned manifold, the decoder should approximately project the latent sample into the learned data manifold  $\mathcal{X}$ . Next, assuming  $\mathcal{X} \approx \mathcal{Z}$ , that is to say, generated samples do not differ from the real samples too much, the encoder projects the generated sample  $\hat{\mathbf{x}}_i$  onto the latent manifold  $\mathcal{Z}$ .

$$\mathbf{R}(\mathbf{z}) = h_{\phi}^{\text{enc}}(h_{\theta}^{\text{dec}}(\mathbf{z})) \quad (2)$$

with the associated distribution,

$$r(\hat{\mathbf{z}} | \mathbf{z}) = \int q_{\phi}(\hat{\mathbf{z}} | \hat{\mathbf{x}}) p_{\theta}(\hat{\mathbf{x}} | \mathbf{z}) d\hat{\mathbf{x}} = \mathbb{E}_{\hat{\mathbf{x}} \sim p_{\theta}(\cdot | \mathbf{z})} [q_{\phi}(\hat{\mathbf{z}} | \hat{\mathbf{x}})] \quad (3)$$

Let  $S : \mathbb{R}^d \mapsto \mathbb{R}$  be the (Euclidean) distance from any point in the latent space to that surface  $\mathcal{Z}$ , i.e.,  $S(\mathbf{z}) = 0$  implies  $\mathbf{z}$  that lies on the manifold, and call it the *latent excitation*. The gradient of this function  $\nabla S$ , then projects any point in the latent space onto the learned manifold.

Under these conditions, the resulting response  $\mathbf{R}(\mathbf{z}) \in \mathcal{Z}$ , consequently,

$$\mathbf{R}(\mathbf{z}) - \mathbf{z} \approx \nabla_{\mathbf{z}} S(\mathbf{z}) \quad (4)$$

Recall that by the definition of the latent excitation  $S$  and the latent manifold  $\mathcal{Z}$  we expect  $S \approx 0$  for all samples  $\mathbf{z} \sim q_{\phi}(\cdot | \mathbf{x})$ , so for  $\nabla S$  to be non-trivial, we implicitly rely on the decoder (and encoder) having a certain degree of robustness with respect to the input. For certain choices of  $\mathbf{z}$  this robustness is not unfounded. The KL regularization in the ELBO encourages the posterior  $q_{\phi}(\mathbf{z} | \mathbf{x})$  to match the prior, so it is not unreasonable to expect for the decoder to be able to handle samples from the prior  $\mathbf{z} \sim p(\cdot)$  even if the samples do not fully match the learned manifold, in fact generating new samples with VAEs relies on this. More generally, [40] have shown autoencoders to be locally contractive near  $\mathcal{Z}$  implying a degree of robustness. To the extent to which we stay near the manifold  $\mathcal{Z}$  and in particular the prior  $p(\mathbf{z})$ , we can use  $\mathbf{R}(\mathbf{z})$  to estimate for  $\nabla S$ , from which we can map out the learned manifold directly.

In our analysis, we develop several tools and metrics using the latent responses illustrated in figure 1 by applying different kinds of interventions in the latent space.

### 4.1 Latent Response Matrix

The first practical tool we introduce based on latent responses is the *Latent Response Matrix* which aims to identify the causal variables of the learned generative process and how they affect one another. The high level procedure is to intervene on individual latent variables at a time and then use the resulting latent response  $\mathbf{R}$  as a stand in for the effect the intervention had in the generated observation space  $\mathcal{X}$ .

We intervene only on the  $j$ th latent dimension of  $\mathbf{z}$ , setting it to some desired value  $v$ , denoted as  $\text{replace}(\mathbf{z}, j, v)$ . The replacement values  $v$  are sampled from the marginal aggregate posterior  $v \sim q_{\phi}^{(j)}(z^{(j)}) = \int q_{\phi}(\mathbf{z} | \mathbf{x}) \pi(\mathbf{x}) d\mathbf{x} dz^{(i)}$  for  $i \in \{1, \dots, d\} \setminus \{j\}$ , so effectively the intervened latent vector is identical to the original one, except that the  $j$ th latent variable is independently resampled. Although the intervention affects only a single latent dimension, the response may affect other dimensions, thereby revealing dependencies between latent variables (see in figure 1 for a conceptual

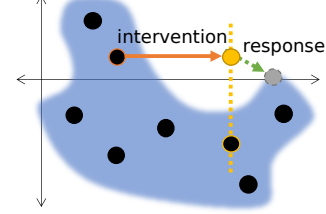


Figure 1: Data points are shown as dark points and complex data manifold in shaded blue. We use the framework of latent responses to find the closest data point which is still on the manifold given an intervention and demonstrate the benefits in improved sampling and model selection techniques.

example). The "effects" are quantified as the root-mean-squared difference between the intervened and unintervened latent sample,

$$M_{jk}^2 = \mathbb{E}_{\mathbf{x} \sim \pi(\cdot); \mathbf{z} \sim q_\phi(\cdot | \mathbf{x}); v \sim q_\phi^{(j)}(\cdot)} [|R_k(\text{replace}(\mathbf{z}, j, v)) - R_k(\mathbf{z})|^2] \quad (5)$$

Each element in the resulting matrix  $M_{jk} \in \mathbb{R}^{d \times d}$  is interpreted as quantifying how much of an effect an intervention on the  $j$ th latent variable has on the  $k$ th variable in the latent space. When the diagonal of the matrix is small (close to 0), it means an intervention on  $z^{(j)}$  does not have an effect recognizable by the encoder, implying the variable is not causal. This allows us to identify the latent variables that are not used by the encoder and ignored by the decoder due to posterior collapse.

On the other hand, if every intervention on  $z_j$  has a corresponding effect, then the response should approach  $\sqrt{2}\sigma(z_j)$  where  $\sigma(z_j)$  is the standard deviation of the marginal distribution of the  $j$ th latent variable (proof in the supplement). In theory  $\sigma(z_j) = 1$  since the prior is a standard normal, however in practice, we observe the KL regularization often compresses the marginal posterior somewhat so that  $\sigma(z_j)$  may be somewhat smaller. To focus on the dependencies between causal variables, we suggest removing the rows and columns corresponding to non-causal latent variables (for our purposes, this includes all dimensions  $j$  for which  $M_{jj} < 0.5$ ), defining  $\tilde{M}_{jk} \in \mathbb{R}^{\tilde{d} \times \tilde{d}}$  where  $\tilde{d} \leq d$  is the number of causal latent variables, and consequently also the intrinsic dimension of the latent manifold, so  $\mathcal{Z} \subseteq \mathbb{R}^{\tilde{d}} \subseteq \mathbb{R}^d$ .

Perhaps even more interesting, the off-diagonal elements of  $M_{jk}$  show to what extent an intervention on causal variable  $j$  affects another  $k$ . When interpreting the latent response matrix as an adjacency matrix in a directed graph, we can visualize the learned structural causal graph. Note that there may, and most likely will, be some cycles in this graph depending on the structure of the latent manifold. For example, the model may learn to embed a periodic factor of variation into two latent dimensions, such as  $j_1$  and  $j_2$ , to keep the representation continuous. In that case, we would expect an intervention along dimension  $j_1$  to elicit a similar response in  $j_2$  as the response of  $j_1$  from an intervention on  $j_2$ . Consequently, in cases where  $M_{j_1 j_2} \approx M_{j_2 j_1} > 0$  it may be useful to treat those latent dimensions as being part of the same latent causal variable, thereby allowing for multi-dimensional causal variables. While the same reasoning naturally holds for higher dimensional groupings (3D, 4D, etc. embeddings of a single factor of variation), for simplicity we shall restrict our analysis here to take 2D embeddings into account.

#### 4.1.1 Conditioned Response Matrix

While the latent response matrix  $M_{jk}$  lets us quantitatively compare how much each latent dimension affects another, thereby teasing out a learned causal model, we have no guarantee that any of the learned causal variables will correspond to the true causal factors [56]. However, if we have access to the true generative process, or at least the true labels  $\mathbf{c}_i$  of the observations  $\mathbf{x}_i$ , then we can use a variant of the latent response matrix, termed the *conditioned response matrix*, to measure how well learned variables matches with the true ones, thereby evaluating the disentanglement of the representation.

The key is to sample observations  $\mathbf{x}$  from a carefully selected subset of the data manifold where only a single true factor  $c^{(m)}$  changes, while all other factors of variation are held constant. To clarify the notation, we write the true generative process as  $g^*(\mathbf{x} | c^{(m)}, \mathbf{c}^{(\setminus m)})$  to separate the  $m$ th true factor  $c^{(m)}$  from the other  $m - 1$  variables denoted  $\mathbf{c}^{(\setminus m)}$ . Now we condition the aggregate posterior  $q_\phi$  and the marginal of the  $j$ th dimension  $q_\phi^{(j)}$  on  $\mathbf{c}^{(\setminus m)}$ , denoted  $q_\phi(\cdot | \mathbf{x}, \mathbf{c}^{(\setminus m)})$  and  $q_\phi^{(j)}(z^{(j)} | \mathbf{c}^{(\setminus m)})$  respectively. All together,

$$M_{mj}^{*2} = \mathbb{E}_{c^{(m)}, \mathbf{c}^{(\setminus m)} \sim g^{**}(\cdot); \mathbf{x} \sim g^*(\cdot | c^{(m)}, \mathbf{c}^{(\setminus m)}); \mathbf{z} \sim q_\phi(\cdot | \mathbf{x}, \mathbf{c}^{(\setminus m)}); v \sim q_\phi^{(j)}(\cdot | \mathbf{c}^{(\setminus m)})} [|R_j(\text{replace}(\mathbf{z}, j, v)) - R_j(\mathbf{z})|^2] \quad (6)$$

By conditioning the posterior to a sub-space of the manifold where only a single true factor of variation varies at a time, when we intervene by resampling the marginal of dimension  $j$ , the latent response tells us whether or not interventions on dimension  $j$  can be expected to affect the true factor of variation  $m$ , so  $M^* \in \mathbb{R}^{d^* \times d}$ . Furthermore, we can once again discard the columns corresponding to the non-causal variables, leaving  $\tilde{M}^* \in \mathbb{R}^{d^* \times \tilde{d}}$ .



#### 4.1.2 Causal Disentanglement Score

This is similar to the *responsibility matrix* introduced by [52], except the responsibility matrix identifies to what extent each latent variable is predictive of (i.e. associated with) each true factor of variation, while the conditioned response matrix identifies the causal structure. Just as [52], we define disentanglement to mean varying each latent variable affects at most one true factor of variation, from which we define the *causal disentanglement score* (CDS) in equation 7. Similarly, we define the "completeness" of a representation in the appendix. As written, the score is between  $\frac{1}{d^*}$  and 1, but we re-scale it to  $[0, 1]$ .

$$\text{CDS} = \frac{\sum_j \max_m M_{mj}^*}{\sum_{mj} M_{mj}^*} \quad (7)$$

#### 4.2 Structure Score

Next we investigate a more general property of representations: structure. While there are a plethora of different types of structure one might study, our focus here is on treating structure as a form of complexity [57–59]. More specifically, how much information needs to be communicated before the likelihood of some sample can be evaluated. For a normal distribution, thanks to the rotational symmetry, you need two numbers (e.g. the standard deviation, and the distance between the sample and the mean). Under this concept of structure, it becomes apparent the standard normal is a particularly unstructured choice for a prior. Since the standard deviation is fixed to 1, there is only a single degree of freedom in the probability density function  $p(\mathbf{x})$ , the magnitude of  $\mathbf{x}$ . Consequently, if the model wants to build more complexity into the latent manifold, it must match the

To quantify the degree to which the posterior matches with the prior, we propose comparing  $r(\hat{\mathbf{z}}) = \int r(\hat{\mathbf{z}} | \mathbf{z}) p(\mathbf{z}) d\mathbf{z}$  to the prior  $p(\mathbf{z})$ . While in principle any metric can be used, we take inspiration from [60] and suggest estimating the Wasserstein distance using the maximum mean discrepancy (MMD) to define the *Structure Score* (SS).

$$\text{SS} = \text{MMD}_k(p, r) = \left\| \int_{\mathcal{Z}} k(z, \cdot) dp(z) - \int_{\mathcal{Z}} k(z, \cdot) dr(z) \right\|_{\mathcal{H}_k} \quad (8)$$

where  $k(\mathbf{z}, \mathbf{z}')$  is a characteristic kernel with corresponding reproducing kernel hilbert space (RKHS)  $\mathcal{H}_k$  (same as [60]).

Note that to estimate the latent response distribution  $r(\mathbf{z})$  all we need are samples from the prior, while if we estimated the difference between the prior and posterior  $q_\phi(\mathbf{z}) = \int q_\phi(\mathbf{z} | \mathbf{x}) \pi(\mathbf{x}) d\mathbf{x}$  directly, we rely on the empirical data distribution  $\pi(\mathbf{x})$ .

Since this score (correctly) treats collapsed latent variables as unstructured, however these variables are non-causal and therefore not relevant for understanding the structure in the learned manifold. Therefore, we suggest a variant of the structure score, *causal structure score*, which only takes the causal latent variables (as defined in section 4.1) into account and entirely ignores (fixes to 0) others.

#### 4.3 2D Maps

The last type of analysis we employ focuses on gaining a qualitative understanding of the learned latent manifold as opposed to describing the representation through quantitative metrics. Specifically, we aim to take advantage of the connection between the latent response function  $\mathbf{R}(\mathbf{z})$  and the latent excitation  $S(\mathbf{z})$ , namely, that  $\mathbf{R}(\mathbf{z}) \approx \nabla S(\mathbf{z})$  near the manifold.

Guided by the latent response matrix, we select identify pairs of latent variables that appear to share some interesting structure. Then we project the whole latent space onto those two dimensions. We split the whole space into a regular 2D grid of points (usually 100x100), and evaluate the response  $\mathbf{R}(\mathbf{z})$  at each point to produce a response field  $\mathbf{F}_{i,j}$

$$\mathbf{F}_{i,j} = \mathbf{R}(\mathbf{z}_{i,j}) - \mathbf{z}_{i,j} \quad (9)$$

where  $\mathbf{z}_{i,j}$  refers to the latent sample at grid index  $i, j$ . Then we numerically estimate the divergence of the response field  $\nabla \cdot \mathbf{F}_{i,j}$  to measure the laplacian and mean curvature of  $S$ , thereby visualizing the learned manifold (details in the supplement).

Note that the grid only intervenes along the two selected latent dimensions, however the response, and thereby also the response field, depends on the whole latent vector. Consequently, we can either

average the response field for over the remaining latent variables, producing a mean field or we can condition the map on a fixed latent sample. The mean field approximation is particularly useful for visualizing the learned manifold and improving sampling, as it focuses on the general shape of the latent manifold.

When interpolating between latent samples  $\mathbf{z}$  on the manifold  $\mathcal{Z}$ , ideally we would like to remain on the learned manifold so the interpolation is meaningful in the ambient space [61]. This corresponds to finding the shortest path between two latent samples  $\mathbf{z}_a$  and  $\mathbf{z}_b$  subject to  $S = 0$  everywhere along the path, or, relaxing that constraint somewhat, we want to minimize  $S$  along the path.

Unfortunately, estimating  $S$  from the responses would require estimating computationally expensive path integrals. Instead, for now, we propose substituting the cost  $S$  for the  $\|\nabla S\|^2$  which can be directly evaluated from the response field. The obvious downside to this scheme is local maxima and minima of  $S$  are indistinguishable to the cost function. However, since any  $\mathbf{z}_a \in \mathcal{Z}$  starts off in a local minimum, we can hope to avoid maxima of  $S$  by setting the search temperature sufficiently low (details in the supplement). We leave the implementation of more sophisticated path planning algorithms for future work [62–64].

## 5 Toy Example: The Double Helix

To illustrate how the latent response framework can be used to study the representation learned by a VAE, we show the process when learning a 2D representation for samples from a double helix embedded in  $\mathbb{R}^3$ .

$$x_i = [A_1 \cos(\pi(\omega t_i + n_i)), A_2 \sin(\pi(\omega t_i + n_i)), A_3 t_i]^T + \epsilon_i \quad (10)$$

where  $t_i \sim \text{Uniform}(-1, 1)$ ,  $n_i \sim \text{Bernoulli}(0.5)$ ,  $\epsilon_i \sim \mathcal{N}(\mathbf{0}, \sigma \mathbf{I})$ . For this experiment, we set  $A_1 = A_2 = A_3 = \omega = 1$  and  $\sigma = 0.1$ . Disregarding the additive noise  $\epsilon_i$ , the data manifold has two degrees of freedom.

Although this analysis is largely independent of the precise neural network architecture, for this experiment we aim to provide the model sufficient capacity to learn a satisfactory representation, so we use four hidden layers with 32 units each. We train until convergence (at most 5k steps) with an Adam optimizer on a total of  $N = 1024$  training samples (see the supplement for training and architecture details).

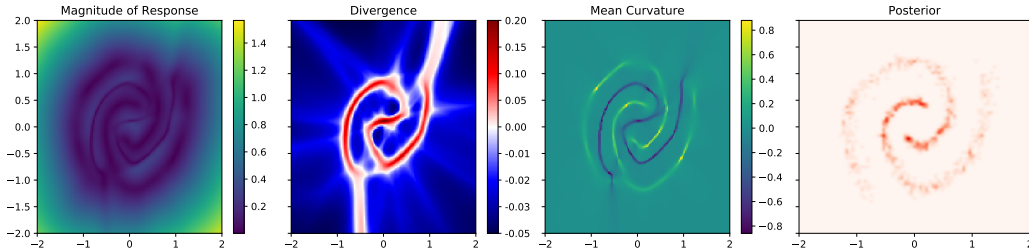


Figure 2: Depicted are three quantities derived using the latent response function to better understand the representation learned by a VAE for the double helix compared to the aggregate posterior shown on the far right. Note that almost all the density of the posterior is in regions that have negative divergence, and consequently positive curvature.

Figure 2 provides an neat example for how the response field maps out the latent representation through the divergence and curvature. Specifically, the divergence focuses on the boundaries (red) is somewhat negative for the majority of space. So we can interpret the blue region as approximating the region where the decoder can projection the latent sample confidently, while positive divergence regions are divergent as the decoding is less precise. The path in red shows the shortest euclidean distance between the two points, however as is clearly seen in the maps in figure 3 and even the posterior density, the red path clearly does not remain on the learned manifold. Finally meanwhile the green path traces the natural path along one strand.

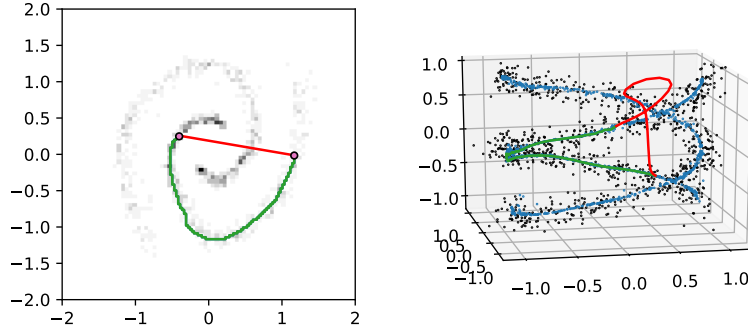


Figure 3: The left plot shows the 2D latent space including the aggregate posterior density in black, and two possible interpolations between the two pink points. Meanwhile, the plot on the right shows the ambient data space with the black points being the observed data samples, the blue points the reconstructed samples, and the paths in the ambient space corresponding to the ones in the latent space. Note how the path in green follows the learned manifold and consequently much more consistent in the ambient space. Meanwhile, the shortest (euclidean) path in the latent space hops between strands twice.

## 6 Experiments and Results

**Experimental Setup** We test our new tools on a small selection of common benchmark datasets, including 3D-Shapes [65], MNIST [66], and Fashion-MNIST [67]<sup>4</sup>. Our methods are directly applicable to any VAE-based model, but can naturally be extended to any autoencoders. Nevertheless, we focus our empirical evaluation on  $\beta$ -VAEs and denote by substituting the  $\beta$  (so 4-VAE refers to a  $\beta$ -VAE where  $\beta = 4$ ). We also investigate to what extent the size of the latent space  $d$  affects the disentanglement and structure. All our models use four convolution and two fully-connected layers in the encoder and decoder. The models are trained using Adam [68] with a learning rate of 0.001 for 100k steps (see supplement for details).

**Qualitative Understanding** Aside from the metrics, which we discuss below, the primary way for us to better understand the manifold structure is the visualization of 2D projections. This is obviously very limiting as it requires information in the representation to mostly be axis-aligned (which is not completely unreasonable for VAEs [25]), but more importantly this may obscure any higher-dimensional structure of the representation. However, for models that do meet these criteria, we can directly observe the complicated structure, such as in figure 4. Note that the decision boundaries between regions is quite narrow so classifying a sample into one of the 10 centers is relatively easy for the model, as evidenced by the negative divergence over most of the region.

From the mean curvature map in figure 5a, we see that the manifold is particularly nonlinear along these two latent dimensions (13 and 14). Consequently, there can be a dramatic difference between the shortest path connecting two points while remaining on the manifold compared to the shortest path in euclidean space as seen in figure 5.

**Causal Structure** Turning to table 1, as expected, the disentanglement is increasing with increasing  $\beta$ . Our proposed CDS score correlates strongly with the other disentanglement metrics. Perhaps noteworthy is that even though the CDS and DCI-D scores are computed in similar ways (the vital difference being whether responsibility rests on a causal link or a correlation), the DCI-D scores are consistently lower than the CDS scores. This may be explained by the DCI-D metric taking additional spurious correlations between latent variables into account, while the CDS metric focuses on the causal links, so the DCI-D has an undeservedly low score.

Digging a little deeper into how the latent response matrix elucidate the causal structure of the representation, figure 6 shows the responsibility matrix matches the conditioned response matrix for the most part. The only exception being latent variables 4 and 20. Since the DCI framework identifies which latent variables are most predictive for the true factors, it cannot distinguish between

<sup>4</sup>All are provided with an MIT, Apache or Creative Commons License

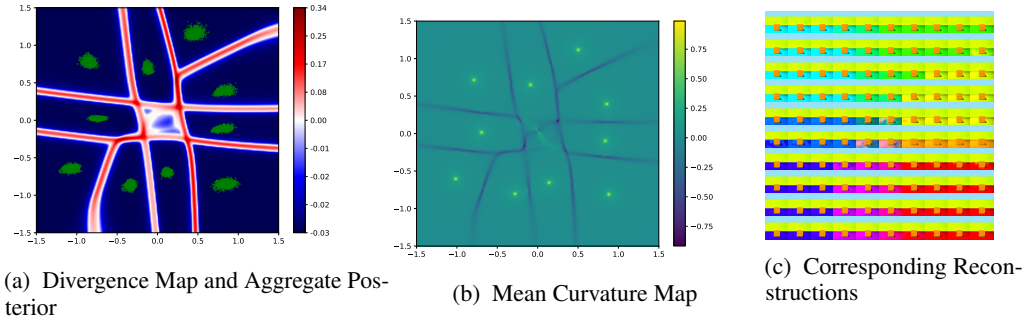


Figure 4: A projection along dimensions 16 (horizontally) and 22 for the same model shown in 6. 4a shows the computed divergence of the response field in blue and red while the green points are samples from the aggregate posterior. 4b shows the resulting mean curvature, which identifies 10 points where the curvature spikes and the boundaries between the regions corresponding to different clusters in the posterior. Finally 4c shows the reconstructions over the same region (with all other latent variables fixed), thereby making it clear that each of the clusters in the posterior corresponds to a different floor hue. Note that, although the aggregate posterior is highly concentrated at a few points, the negative divergence almost everywhere suggests the decoder can still generate high fidelity samples over most of the subspace, which is confirmed by the corresponding reconstructions.

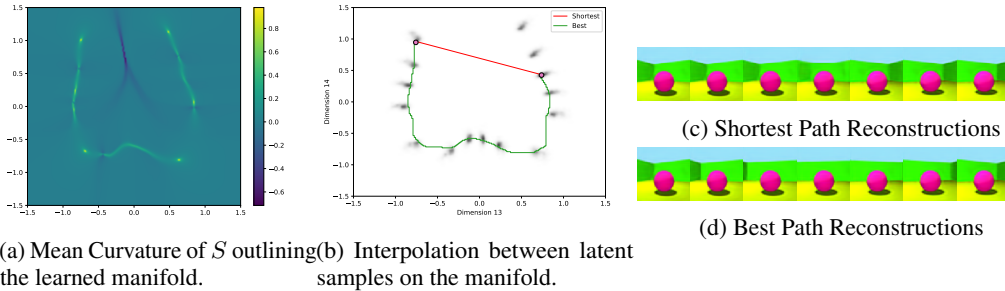


Figure 5: Using the same 4-VAE model trained on 3D-Shapes as in figure 6, and a similar setting figure 3, we now search for the shortest path along the latent manifold, visualized in 5a. between two samples from the posterior. Figure 5b compares this best path (in green) to the shortest path in euclidean distance (in red), and we see good agreement between the best path and the aggregate posterior (the grey density). Finally, to get a better sense for how a *meaningful* interpolation differs from a naive one, we decode the samples at evenly spaced intervals for each of the paths shown in 5c and 5d.

Name	CDS	DCI-D	IRS	MIG
1-VAE	0.44	0.3	0.44	0.07
2-VAE	0.49	0.36	0.46	0.09
4-VAE	0.58	0.46	0.51	0.16
8-VAE	0.71	0.66	0.63	0.21
1-VAE	0.52	0.49	0.48	0.09
2-VAE	0.61	0.58	0.52	0.15
4-VAE	0.72	0.67	0.57	0.17
8-VAE	0.78	0.73	0.64	0.2

Table 1: Comparing disentanglement metrics for VAEs trained on 3D-shapes with varying  $\beta$ . For the models in the first four rows  $d = 12$ , while  $d = 24$  for the remaining four. Interestingly, we see that the DCI-D disentanglement score increases significantly when doubling the latent space size, unlike the other metrics. Quantities are averaged over two random seeds.

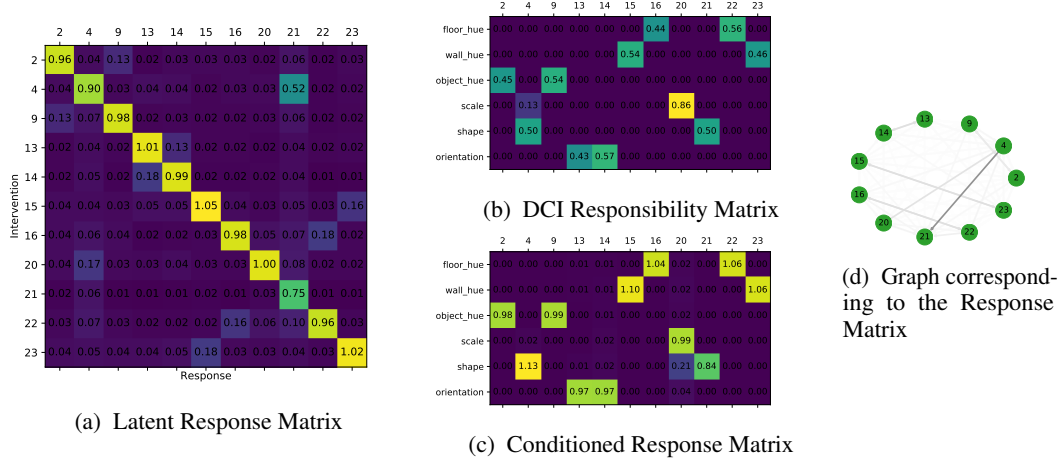


Figure 6: These are the (6a) latent response matrix, (6b) DCI Responsibility matrix [52], (6c) conditioned response matrix, and the (6d) derived from the latent response matrix for a 4-VAE ( $d = 24$ ) trained on 3D-Shapes. The responsibility matrix shows the predictability of each latent dimension (column) for each factor of variation (row), while the conditioned response matrix measures the effect an intervention in each latent dimension (column) has given that the intervention can only change one factor of variation (row). Note that from the conditional response matrix we can confirm that all of the information pertaining to the camera angle is contained in dimensions 13 and 14, which justifies our projection onto 13 and 14 for interpolation as discussed in figure 5.

Model	MNIST	Fashion-MNIST	3D-Shapes	MPI3D-Toy	MPI3D-Real
1-VAE	$4.9 \pm 1.3$	$1.5 \pm 0.7$	$36 \pm 2$	$3.1 \pm 1.4$	$8 \pm 2$
2-VAE	$1.6 \pm 0.6$	$1.1 \pm 0.3$	$33 \pm 3$	$0.8 \pm 0.4$	$2.9 \pm 0.2$
4-VAE	$0.7 \pm 0.4$	$1.1 \pm 0.4$	$32 \pm 1$	$0.15 \pm 0.04$	$2.0 \pm 1$
8-VAE	$0.5 \pm 0.2$	$0.9 \pm 0.1$	$23 \pm 9$	$0.05 \pm 0.02$	$0.4 \pm 0.3$

Table 2: Evaluating our proposed Structure Score  $SS$  ( $\times 1000$ ) with 95% confidence intervals from 3 random seeds. As expected, the harsh regularization and possible posterior collapse as  $\beta$  increases results in a decrease in the structure score. However, the large intervals suggest the degree to which representations can be more structured is rather sensitive to the random seed.

a correlation and a causal link. In this case, the DCI metric recognized a correlation between dimension 4 and the "scale" factor. However, from the latent response matrix (and the graph 6d) we see interventions on dim 20 have a significant effect on dim 4, but not vice versa. Consequently, we identify dim 20 is a parent of dim 4 in the learned causal graph. Since dim 20 is closely related with the "scale" factor the causal link to dim 4 results in dim 4 being correlated with "scale". The conditioned response matrix correctly identifies that it is dimension 20 which primarily affects the scale, but indirectly also affects the shape through dimension 4. This is a prime example of how causal reasoning can avoid misattributing responsibility due to spurious correlations.

**Structure Score Evaluation** Finally, table 2 compares the structure scores for all datasets we consider. Particularly noteworthy is that 3D-Shapes consistently produces significantly more structured manifolds than other datasets. Since the model architecture and training hyperparameters are common for all datasets, the structure scores give us a sense for how well the underlying true generative processes can be modeled with the inductive biases in our method. This metric also allows us to directly measure the effect of stronger regularization (increasing  $\beta$ ), which helps identify the optimal trade-off between matching the prior and sample fidelity.

## 7 Conclusion

In this work we have introduced and formalized the latent response framework including a variety of tools to better visualize and understand the representations learned by variational autoencoders. The

current analysis relies on a certain degree of (axis-aligned) structure in the latent space to become apparent and currently only works for *local* interventions [40]. This has close connections to learning disentangled representations [53] and future work can thus utilize the large literature and ongoing research on learning disentangled representations as well as investigate if the estimation procedure can be done on-the-fly and even be used as a regularization technique during training.

## Acknowledgements

This work was supported by the German Federal Ministry of Education and Research (BMBF): Tübingen AI Center, FKZ: 01IS18039B, and by the Machine Learning Cluster of Excellence, EXC number 2064/1 – Project number 390727645. The authors thank the International Max Planck Research School for Intelligent Systems (IMPRS-IS) for supporting Felix Leeb.

## References

- [1] David E Rumelhart, Geoffrey E Hinton, and Ronald J Williams. Learning internal representations by error propagation. Technical report, California Univ San Diego La Jolla Inst for Cognitive Science, 1985.
- [2] Dana H Ballard. Modular learning in neural networks. In *AAAI*, pages 279–284, 1987.
- [3] Diederik P. Kingma and Max Welling. Auto-encoding variational Bayes, 2013. URL [arXiv:1312.6114](https://arxiv.org/abs/1312.6114).
- [4] Ali Razavi, Aaron van den Oord, and Oriol Vinyals. Generating diverse high-fidelity images with vq-vae-2. *arXiv preprint arXiv:1906.00446*, 2019.
- [5] James Townsend, Tom Bird, and David Barber. Practical lossless compression with latent variables using bits back coding. *arXiv preprint arXiv:1901.04866*, 2019.
- [6] Jinwon An and Sungzoon Cho. Variational autoencoder based anomaly detection using reconstruction probability. *Special Lecture on IE*, 2(1):1–18, 2015.
- [7] Jiwei Li, Minh-Thang Luong, and Dan Jurafsky. A hierarchical neural autoencoder for paragraphs and documents. *arXiv preprint arXiv:1506.01057*, 2015.
- [8] Rewon Child. Very deep vaes generalize autoregressive models and can outperform them on images. *arXiv preprint arXiv:2011.10650*, 2020.
- [9] Đorđe Miladinović, Aleksandar Stanić, Stefan Bauer, Jürgen Schmidhuber, and Joachim M Buhmann. Spatial dependency networks: Neural layers for improved generative image modeling. *International Conference on Learning Representations (ICLR)*, 2021.
- [10] Yoshua Bengio, Aaron Courville, and Pascal Vincent. Representation learning: A review and new perspectives, 2012. URL [arXiv:1206.5538](https://arxiv.org/abs/1206.5538).
- [11] SM Ali Eslami, Danilo Jimenez Rezende, Frederic Besse, Fabio Viola, Ari S Morcos, Marta Garnelo, Avraham Ruderman, Andrei A Rusu, Ivo Danihelka, Karol Gregor, et al. Neural scene representation and rendering. *Science*, 360(6394):1204–1210, 2018.
- [12] Ankesh Anand, Evan Racah, Sherjil Ozair, Yoshua Bengio, Marc-Alexandre Côté, and R Devon Hjelm. Unsupervised state representation learning in atari. *arXiv preprint arXiv:1906.08226*, 2019.
- [13] Andrea Dittadi, Frederik Träuble, Francesco Locatello, Manuel Wüthrich, Vaibhav Agrawal, Ole Winther, Stefan Bauer, and Bernhard Schölkopf. On the transfer of disentangled representations in realistic settings. *arXiv preprint arXiv:2010.14407*, 2020.
- [14] Aravind Srinivas, Michael Laskin, and Pieter Abbeel. Curl: Contrastive unsupervised representations for reinforcement learning. *arXiv preprint arXiv:2004.04136*, 2020.

- [15] Bernhard Schölkopf, Francesco Locatello, Stefan Bauer, Nan Rosemary Ke, Nal Kalchbrenner, Anirudh Goyal, and Yoshua Bengio. Toward causal representation learning. *Proceedings of the IEEE*, 109(5):612–634, 2021.
- [16] Michael M Bronstein, Joan Bruna, Yann LeCun, Arthur Szlam, and Pierre Vandergheynst. Geometric deep learning: going beyond euclidean data. *IEEE Signal Processing Magazine*, 34(4):18–42, 2017.
- [17] Federico Monti, Davide Boscaini, Jonathan Masci, Emanuele Rodola, Jan Svoboda, and Michael M Bronstein. Geometric deep learning on graphs and manifolds using mixture model cnns. In *Proceedings of the IEEE conference on computer vision and pattern recognition*, pages 5115–5124, 2017.
- [18] Christos Louizos, Kevin Swersky, Yujia Li, Max Welling, and Richard Zemel. The variational fair autoencoder. *arXiv preprint arXiv:1511.00830*, 2015.
- [19] Francesco Locatello, Gabriele Abbati, Thomas Rainforth, Stefan Bauer, Bernhard Schölkopf, and Olivier Bachem. On the fairness of disentangled representations. In *Advances in Neural Information Processing Systems*, pages 14584–14597, 2019.
- [20] Justin Ker, Lipo Wang, Jai Rao, and Tchoyoson Lim. Deep learning applications in medical image analysis. *Ieee Access*, 6:9375–9389, 2017.
- [21] Xiaoran Chen, Nick Pawlowski, Martin Rajchl, Ben Glocker, and Ender Konukoglu. Deep generative models in the real-world: An open challenge from medical imaging. *arXiv preprint arXiv:1806.05452*, 2018.
- [22] Diederik P Kingma and Max Welling. Auto-encoding variational bayes. *arXiv preprint arXiv:1312.6114*, 2013.
- [23] Danilo Jimenez Rezende, Shakir Mohamed, and Daan Wierstra. Stochastic backpropagation and approximate inference in deep generative models. *arXiv preprint arXiv:1401.4082*, 2014.
- [24] Irina Higgins, Loic Matthey, Arka Pal, Christopher Burgess, Xavier Glorot, Matthew Botvinick, Shakir Mohamed, and Alexander Lerchner. beta-VAE: Learning basic visual concepts with a constrained variational framework. *ICLR*, 2(5):6, 2017. URL <https://pdfs.semanticscholar.org/a902/26c41b79f8b06007609f39f82757073641e2.pdf>.
- [25] Christopher P Burgess, Irina Higgins, Arka Pal, Loic Matthey, Nick Watters, Guillaume Desjardins, and Alexander Lerchner. Understanding disentangling in  $\beta$ -VAE. *arXiv preprint arXiv:1804.03599*, 2018.
- [26] Pierre Baldi and Kurt Hornik. Neural networks and principal component analysis: Learning from examples without local minima. *Neural networks*, 2(1):53–58, 1989.
- [27] Daniel Kunin, Jonathan Bloom, Aleksandrina Goeva, and Cotton Seed. Loss landscapes of regularized linear autoencoders. In *International Conference on Machine Learning*, pages 3560–3569. PMLR, 2019.
- [28] Michael E Tipping and Christopher M Bishop. Probabilistic principal component analysis. *Journal of the Royal Statistical Society: Series B (Statistical Methodology)*, 61(3):611–622, 1999.
- [29] Shengjia Zhao, Jiaming Song, and Stefano Ermon. Towards deeper understanding of variational autoencoding models. *arXiv preprint arXiv:1702.08658*, 2017.
- [30] Alexander Camuto, Matthew Willetts, Stephen Roberts, Chris Holmes, and Tom Rainforth. Towards a theoretical understanding of the robustness of variational autoencoders. In *International Conference on Artificial Intelligence and Statistics*, pages 3565–3573. PMLR, 2021.
- [31] Chris Cremer, Xuechen Li, and David Duvenaud. Inference suboptimality in variational autoencoders. In *International Conference on Machine Learning*, pages 1078–1086. PMLR, 2018.

- [32] Serena Yeung, Anitha Kannan, Yann Dauphin, and Li Fei-Fei. Tackling over-pruning in variational autoencoders. *arXiv preprint arXiv:1706.03643*, 2017.
- [33] Sebastian J Wetzel. Unsupervised learning of phase transitions: From principal component analysis to variational autoencoders. *Physical Review E*, 96(2):022140, 2017.
- [34] Michal Rolínek, Dominik Zietlow, and Georg Martius. Variational autoencoders pursue pca directions (by accident). In *Proceedings of the IEEE/CVF Conference on Computer Vision and Pattern Recognition*, pages 12406–12415, 2019.
- [35] Shujian Yu and Jose C Principe. Understanding autoencoders with information theoretic concepts. *Neural Networks*, 117:104–123, 2019.
- [36] Shengjia Zhao, Jiaming Song, and Stefano Ermon. InfoVAE: Information maximizing variational autoencoders. *arXiv preprint arXiv:1706.02262*, 2017.
- [37] James Lucas, George Tucker, Roger Grosse, and Mohammad Norouzi. Understanding posterior collapse in generative latent variable models. 2019.
- [38] Danilo Jimenez Rezende and Fabio Viola. Taming VAEs. *arXiv preprint arXiv:1810.00597*, 2018.
- [39] Aican Bozkurt, Babak Esmaeili, Jean-Baptiste Tristan, Dana Brooks, Jennifer Dy, and Jan-Willem Meent. Rate-regularization and generalization in variational autoencoders. In *International Conference on Artificial Intelligence and Statistics*, pages 3880–3888. PMLR, 2021.
- [40] Adityanarayanan Radhakrishnan, Karren Yang, Mikhail Belkin, and Caroline Uhler. Memorization in overparameterized autoencoders. *arXiv preprint arXiv:1810.10333*, 2018.
- [41] A Taylan Cemgil, Sumedh Ghaisas, Krishnamurthy Dvijotham, Sven Gowal, and Pushmeet Kohli. Autoencoding variational autoencoder. *arXiv preprint arXiv:2012.03715*, 2020.
- [42] Martin Heusel, Hubert Ramsauer, Thomas Unterthiner, Bernhard Nessler, and Sepp Hochreiter. Gans trained by a two time-scale update rule converge to a local nash equilibrium. In *Advances in neural information processing systems*, 2017.
- [43] Tim Salimans, Ian Goodfellow, Wojciech Zaremba, Vicki Cheung, Alec Radford, and Xi Chen. Improved techniques for training GANs. In *Advances in neural information processing systems*, pages 2234–2242, 2016.
- [44] Mehdi SM Sajjadi, Olivier Bachem, Mario Lucic, Olivier Bousquet, and Sylvain Gelly. Assessing generative models via precision and recall. *arXiv preprint arXiv:1806.00035*, 2018.
- [45] Tuomas Kynkäänniemi, Tero Karras, Samuli Laine, Jaakko Lehtinen, and Timo Aila. Improved precision and recall metric for assessing generative models. *arXiv preprint arXiv:1904.06991*, 2019.
- [46] Antti Honkela and Harri Valpola. Variational learning and bits-back coding: an information-theoretic view to bayesian learning. *IEEE transactions on Neural Networks*, 15(4):800–810, 2004.
- [47] Yangjun Ruan, Karen Ullrich, Daniel Severo, James Townsend, Ashish Khisti, Arnaud Doucet, Alireza Makhzani, and Chris J Maddison. Improving lossless compression rates via monte carlo bits-back coding. *arXiv preprint arXiv:2102.11086*, 2021.
- [48] Hyunjik Kim and Andriy Mnih. Disentangling by factorising. *arXiv preprint arXiv:1802.05983*, 2018. URL <https://arxiv.org/pdf/1802.05983.pdf>.
- [49] Ricky TQ Chen, Xuechen Li, Roger Grosse, and David Duvenaud. Isolating sources of disentanglement in variational autoencoders. *arXiv preprint arXiv:1802.04942*, 2018.
- [50] Karl Ridgeway and Michael C Mozer. Learning deep disentangled embeddings with the f-statistic loss. *arXiv preprint arXiv:1802.05312*, 2018.





- [70] Sharon Zhou, Eric Zelikman, Fred Lu, Andrew Y Ng, and Stefano Ermon. Evaluating the disentanglement of deep generative models through manifold topology. *arXiv preprint arXiv:2006.03680*, 2020.
- [71] Jan Stühmer, Richard Turner, and Sebastian Nowozin. Independent subspace analysis for unsupervised learning of disentangled representations. In *International Conference on Artificial Intelligence and Statistics*, pages 1200–1210. PMLR, 2020.
- [72] Paul K Rubenstein, Bernhard Schoelkopf, and Ilya Tolstikhin. On the latent space of Wasserstein auto-encoders. *arXiv preprint arXiv:1802.03761*, 2018.
- [73] Jun Han, Martin Renqiang Min, Ligong Han, Li Erran Li, and Xuan Zhang. Disentangled recurrent wasserstein autoencoder. *arXiv preprint arXiv:2101.07496*, 2021.
- [74] Yoshua Bengio, Aaron Courville, and Pascal Vincent. Representation learning: A review and new perspectives. *IEEE transactions on pattern analysis and machine intelligence*, 35(8): 1798–1828, 2013.
- [75] Georgios Arvanitidis, Søren Hauberg, Philipp Hennig, and Michael Schober. Fast and robust shortest paths on manifolds learned from data. In *The 22nd International Conference on Artificial Intelligence and Statistics*, pages 1506–1515. PMLR, 2019.
- [76] Dimitris Kalatzis, David Eklund, Georgios Arvanitidis, and Søren Hauberg. Variational autoencoders with riemannian brownian motion priors. *arXiv preprint arXiv:2002.05227*, 2020.
- [77] Tim R Davidson, Luca Falorsi, Nicola De Cao, Thomas Kipf, and Jakub M Tomczak. Hyper-spherical variational auto-encoders. *arXiv preprint arXiv:1804.00891*, 2018.
- [78] Luca Falorsi, Pim de Haan, Tim R Davidson, Nicola De Cao, Maurice Weiler, Patrick Forré, and Taco S Cohen. Explorations in homeomorphic variational auto-encoding. *arXiv preprint arXiv:1807.04689*, 2018.
- [79] Tong Lin and Hongbin Zha. Riemannian manifold learning. *IEEE Transactions on Pattern Analysis and Machine Intelligence*, 30(5):796–809, 2008.
- [80] Alessandra Tosi, Søren Hauberg, Alfredo Vellido, and Neil D Lawrence. Metrics for probabilistic geometries. *arXiv preprint arXiv:1411.7432*, 2014.

## A Appendix

### A.1 Autoencoders

In the most general setting, all we have access to is a dataset  $\mathcal{D}$  of  $N$  *i.i.d.* samples, a.k.a. observations  $\mathbf{x}_i \in \mathcal{X} \subseteq \mathbb{R}^D$  generated by some unknown stochastic generative process, where the statistical manifold  $\mathcal{X}$  can be effectively approximated by  $d \ll D$  degrees of freedom (so the intrinsic dimension of the data manifold  $d^* \leq d$ ).

More formally, let  $g^*(\mathbf{x} | \mathbf{c})$  be the true generative process, generating observations  $\mathbf{x}$  from the label  $\mathbf{c} \in \mathcal{C} \subseteq \mathbb{R}^{d^*}$ . Together with the underlying true structural causal model [69]  $g^{**}(\mathbf{c})$  or equivalently  $g^{**}(c^{(m)}, \mathbf{c}^{(\setminus m)})$ , we may define the dataset  $\mathcal{D}$ ,

$$\mathcal{D} = \{\mathbf{x}_i | \mathbf{x}_i \sim g^*(\cdot | \mathbf{c}_i), \mathbf{c}_i \sim g^{**}(\cdot)\}_{i=1}^N \quad (11)$$

Now, we train a deep encoder  $h_\phi^{\text{enc}} : \mathbb{R}^D \mapsto \mathcal{Z}$  with trainable parameters  $\phi$  to encode the observation  $\mathbf{z}_i \leftarrow h_\phi^{\text{enc}}(\mathbf{x}_i)$  into a relatively low dimensional latent vector  $\mathbf{z}_i \in \mathcal{Z} \subseteq \mathbb{R}^d$ , and a decoder  $h_\theta^{\text{dec}} : \mathbb{R}^d \mapsto \hat{\mathcal{X}}$  with parameters  $\theta$  to reconstruct the observations  $\hat{\mathbf{x}}_i \leftarrow h_\theta^{\text{dec}}(\mathbf{z}_i)$ . The primary training objective is to minimize the reconstruction loss, that is to say, to minimize the difference between the true data manifold  $\mathcal{X}$  and the learned data manifold  $\hat{\mathcal{X}}$ . However, note that even after training has converged, the lack of guarantees in the non-convex optimization of deep models, makes it challenging to quantify how much  $\mathcal{X}$  and  $\hat{\mathcal{X}}$  match [41].

### A.2 Matching a Prior Distribution

Many variational autoencoding based methods focus on matching the distribution in the latent space to a known prior distribution by regularizing the reconstruction training objective [55, 70]. Although this structure is convenient for generative modeling and even tends to disentangle the latent space to some extent, it comes at the cost of somewhat blurry images due to posterior collapse and holes in the latent space due to the tradoff between reconstruction quality and matching the prior [56, 24, 25, 48, 71]. To mitigate the double-edged nature of VAEs, less aggressive regularization techniques have been proposed such as the Wasserstein Autoencoder (WAE), which focuses on the aggregate posterior [60]. Unfortunately, WAEs generally fail to produced a particularly meaningful or disentangled latent space [72], unless weak supervision is available [73].

### A.3 The Latent Manifold

**Manifold Learning** The geometry of learned representations with a focus on the generalization ability of neural networks has been discussed in [74]. One key problem is that the standard Gaussian prior used in variational autoencoders relies on the usual Lebesgue measure which in turn, assumes a Euclidean structure over the latent space. This has been demonstrated to lead to difficulties in particular when interpolating in the latent space [61, 75, 76] due to a manifold mismatch [77, 78]. Given the complexity of the underlying data manifold, a viable alternative is based on riemanian geometry [79] which has previously been investigated for alternative probabilistic models like Gaussian Process regression [80].

From a more geometric perspective, we can think of the encoder outputs  $\mathcal{Z} = \{\mathbf{z}_i | \mathbf{z}_i \leftarrow h_\phi^{\text{enc}}(\mathbf{x}_i), \mathbf{x}_i \in \mathcal{X}\}$  as defining a smooth surface in the latent space. Let  $S : \mathbb{R}^d \mapsto \mathbb{R}$  be the (euclidean) distance from any point in the latent space to that surface  $\mathcal{Z}$ , such that  $S(\mathbf{z}) = 0$  implies  $\mathbf{z}$  lies on the manifold, and call it the *latent excitation*. The gradient of this function  $\nabla S$ , then projects any point in the latent space onto the learned manifold. Furthermore, we can compute the laplacian and the related mean curvature 12, which can be interpreted as identifying the regions in the latent space where the  $S$  converges and diverges. Specifically, as  $|\nabla S|$  decreases, if  $\nabla^2 S < 0$ , then you are approaching a local minimum in  $S$ , which implies positive curvature, while  $\nabla^2 S > 0$  surrounds a local maximum.

$$\nabla^2 S = \nabla \cdot \nabla S \quad H = -\frac{1}{2} \nabla \cdot \left( \frac{\nabla S}{|\nabla S|} \right) \quad (12)$$

For VAEs, we can use  $S$  to estimate how well the prior matches the latent manifold and associated aggregate posterior  $\mathcal{Z}$ . Unfortunately, in practice computing  $S$  for arbitrary points in the encoder

is an intractable problem as it would require inverting the encoder. However, as the decoder does approximately invert the encoder, we may still be able to extract information about  $S$ . Specifically, the *locally contractive* structure [40] of trained autoencoders suggest as long as  $\mathbf{z}$  is near the learned manifold, the decoder is able to project the latent sample to the learned support  $\mathcal{X}$ .

## A.4 Latent Responses

### A.4.1 Causal Completeness Score

We define the "completeness" of a representation analogously to [52], that is to say: every true factor of variation is entirely embedded in a single latent dimension. The *causal completeness score* (CCS) follows naturally (scaled to  $[0, 1]$  from  $[\frac{1}{d}, 1]$ ),

$$\text{CCS} = \frac{\sum_m \max_j M_{mj}^*}{\sum_{mj} M_{mj}^*} \quad (13)$$

### A.4.2 Architecture and Training Details

All our models are based on the same convolutional neural network architecture detailed in table 9 so that in total models have approximately 500k trainable parameters. For the smaller datasets MNIST and Fashion-MNIST, samples are upsampled to 32x32 pixels from their original 28x28 and the one convolutional block is removed from both the encoder and decoder.

The datasets are split into a 70-10-20 train-val-test split, and are optimized using Adam [68] with a learning rate of 0.0001, weight decay 0, and  $\beta_1, \beta_2$  of 0.9 and 0.999 respectively. The models are trained for 100k iterations with a batch size of 64 (128 for MNIST and Fashion-MNIST).

Input 64x64x3 image
Conv Layer (64 filters, k=5x5, s=1x1, p=2x2)
Max pooling (filter 2x2, s=2x2)
Group Normalization (8 groups, affine)
ELU activation
Conv Layer (64 filters, k=3x3, s=1x1, p=1x1)
Max pooling (filter 2x2, s=2x2)
Group Normalization (8 groups, affine)
ELU activation
Conv Layer (64 filters, k=3x3, s=1x1, p=1x1)
Max pooling (filter 2x2, s=2x2)
Group Normalization (8 groups, affine)
ELU activation
Conv Layer (64 filters, k=3x3, s=1x1, p=1x1)
Max pooling (filter 2x2, s=2x2)
Group Normalization (8 groups, affine)
ELU activation
Conv Layer (64 filters, k=3x3, s=1x1, p=1x1)
Max pooling (filter 2x2, s=2x2)
Group Normalization (8 groups, affine)
ELU activation
Fully-connected Layer (256 units)
ELU activation
Fully-connected Layer (128 units)
ELU activation
Fully-connected Layer (2d units)
Output posterior $\mu$ and $\log \sigma$

Figure 7: Encoder Architecture

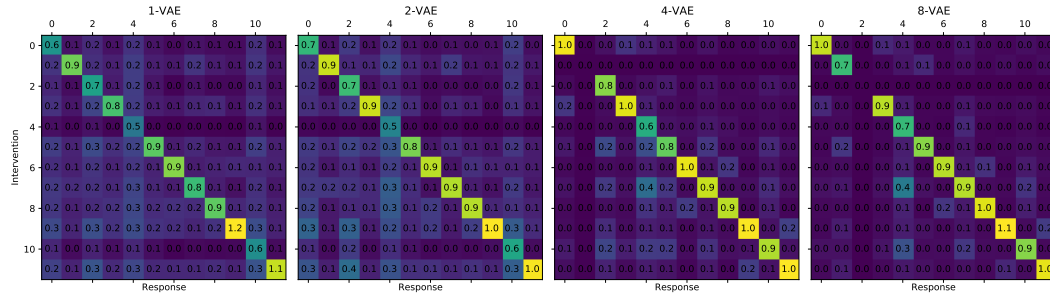
Input $d$ latent vector
Fully-connected Layer (128 units)
ELU activation
Fully-connected Layer (256 units)
ELU activation
Fully-connected Layer (256 units)
ELU activation
Bilinear upsampling (scale 2x2)
Conv Layer (64 filters, k=3x3, s=1x1, p=1x1)
Group Normalization (8 groups, affine)
ELU activation
Bilinear upsampling (scale 2x2)
Conv Layer (64 filters, k=3x3, s=1x1, p=1x1)
Group Normalization (8 groups, affine)
ELU activation
Bilinear upsampling (scale 2x2)
Conv Layer (64 filters, k=3x3, s=1x1, p=1x1)
Group Normalization (8 groups, affine)
ELU activation
Bilinear upsampling (scale 2x2)
Conv Layer (64 filters, k=3x3, s=1x1, p=1x1)
Group Normalization (8 groups, affine)
ELU activation
Conv Layer (3 filters, k=3x3, s=1x1, p=1x1)
Sigmoid activation
Output 64x64x3 image

Figure 8: Decoder Architecture

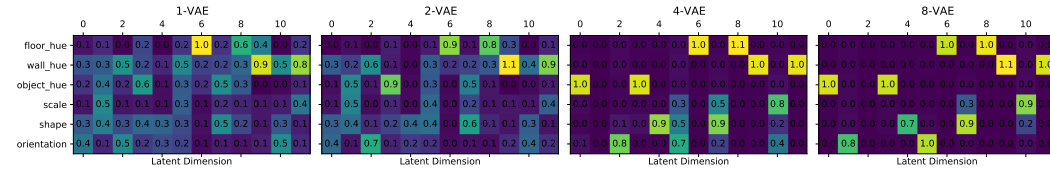
Figure 9: Model architectures where "k" is the kernel size, "s" is the stride, and "p" is the zero-padding

## B Additional Results

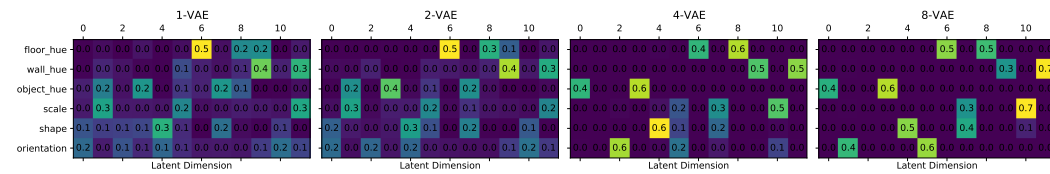
### B.1 3D-Shapes



(a) Latent Response Matrices

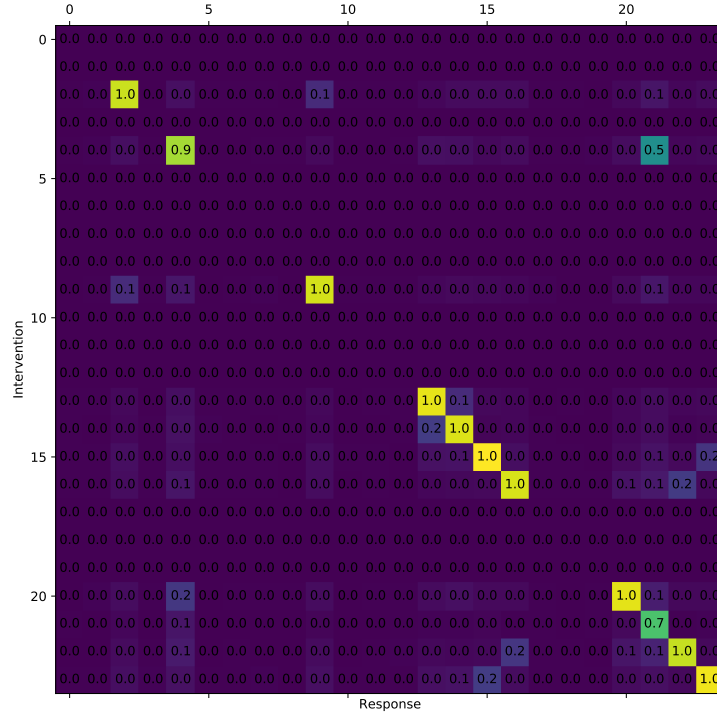


(b) Conditioned Response Matrices

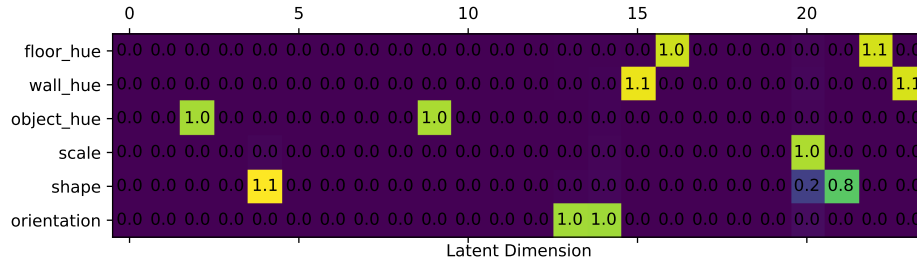


(c) DCI Responsibility Matrices

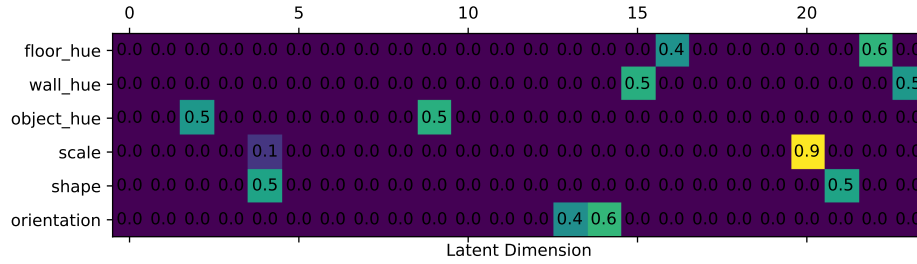
Figure 10: Response and Responsibility matrices for several VAEs ( $d = 12$ ).



(a) Latent Response Matrix



(b) Conditioned Response Matrix



(c) DCI Responsibility Matrix

Figure 11: Full response and responsibility matrices of the 4-VAE ( $d = 24$ ) also shown in figure 6. Note how the Latent Response matrices (11a) shows a categorical difference between the latent dimensions where the diagonal element is close to zero (non-causal), compared to the dimensions with diagonal elements close to 1 (causal).

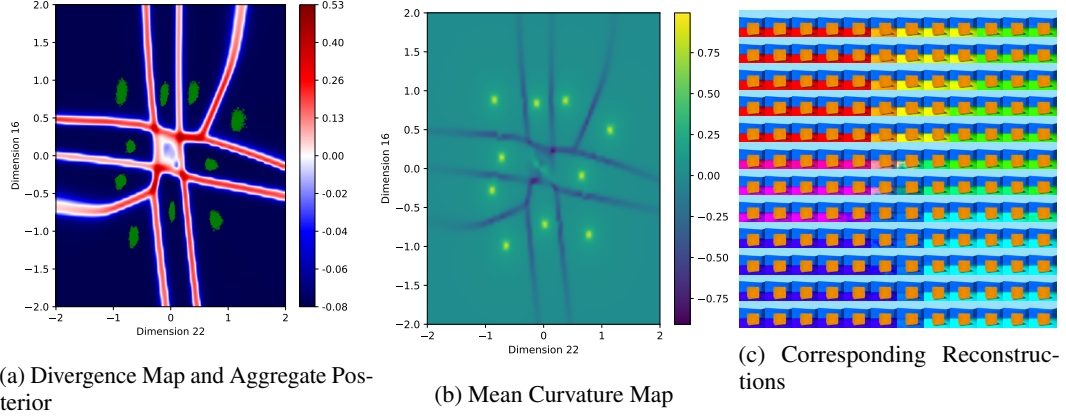


Figure 12: Visualization of the representation learned by a 4-VAE trained on 3D-Shapes (same model as in figure 11).

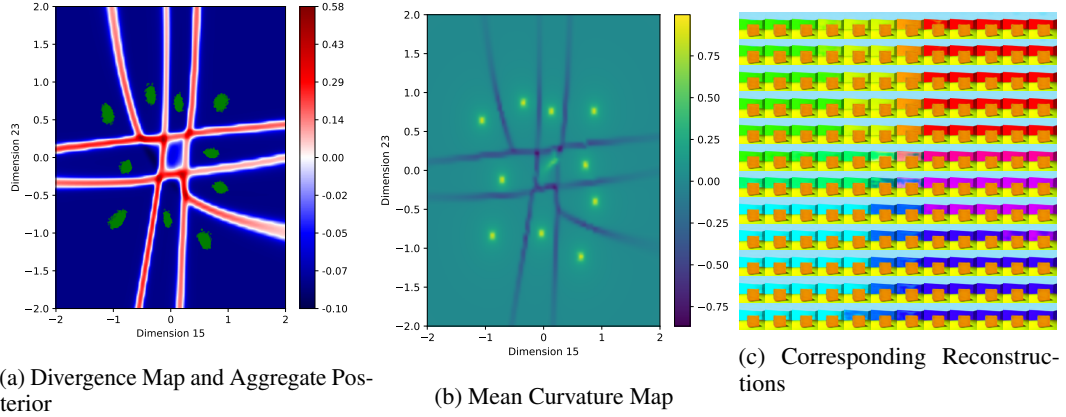


Figure 13: Visualization of the representation learned by a 4-VAE trained on 3D-Shapes (same model as in figure 11).

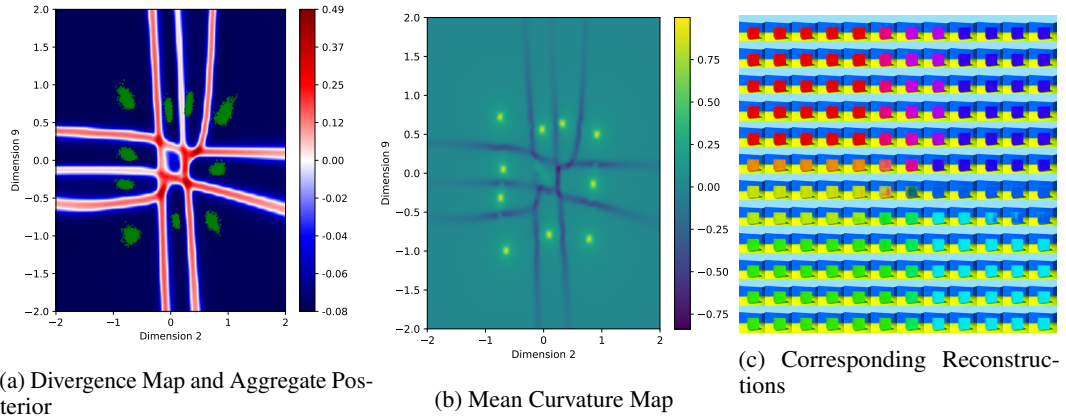


Figure 14: Visualization of the representation learned by a 4-VAE trained on 3D-Shapes (same model as in figure 11).

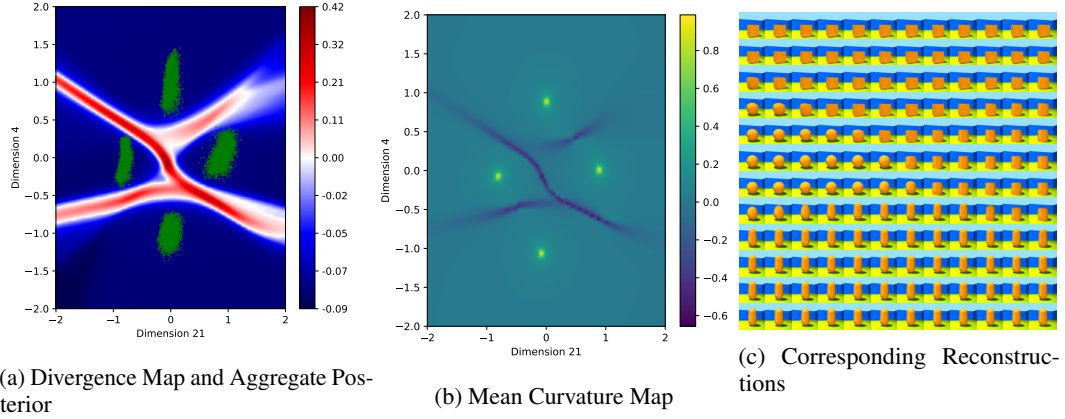


Figure 15: Visualization of the representation learned by a 4-VAE trained on 3D-Shapes (same model as in figure 11). This projection is particularly interesting as the information encoding shape is not exactly axis-aligned, leading to a slight mismatch between the aggregate posterior and the divergence maps. As our visualizations are presently confined to two dimensions, the structure can become significantly more obscured to us if the information is not disentangled and axis-aligned.

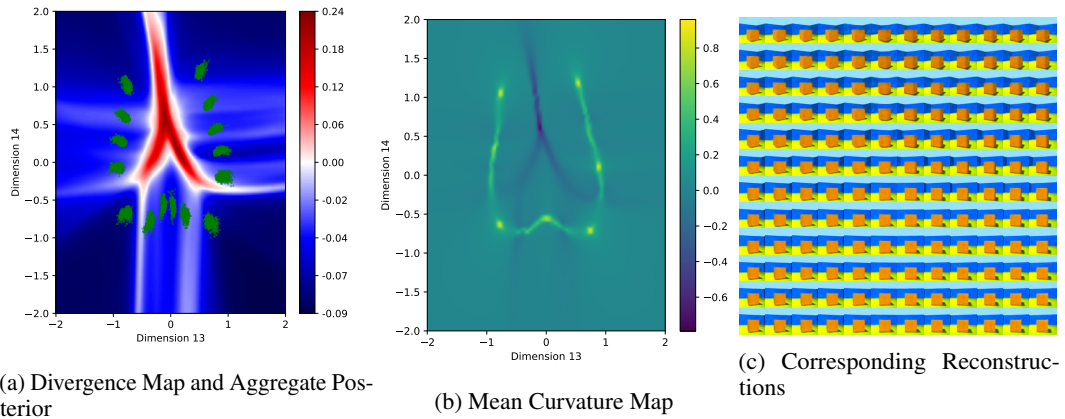
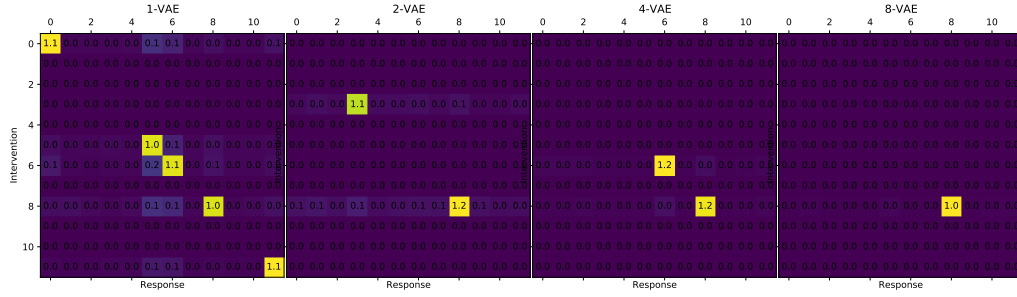


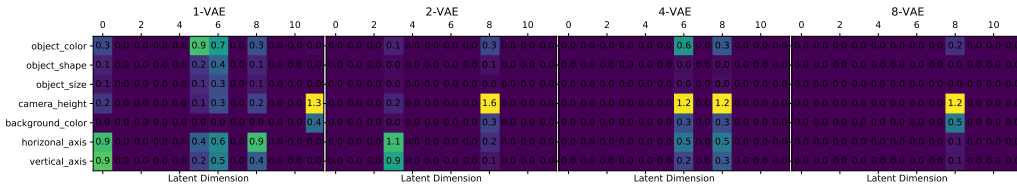
Figure 16: Visualization of the representation learned by a 4-VAE trained on 3D-Shapes (same model as in figure 11).



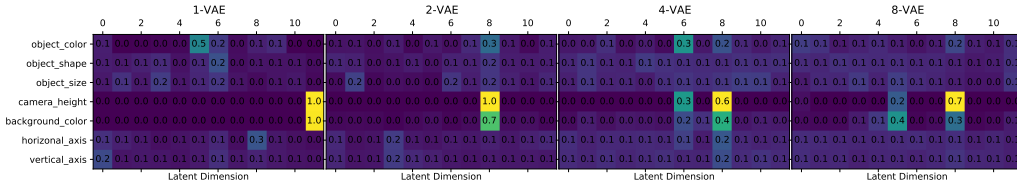
## B.2 MPI3D



(a) Latent Response Matrices

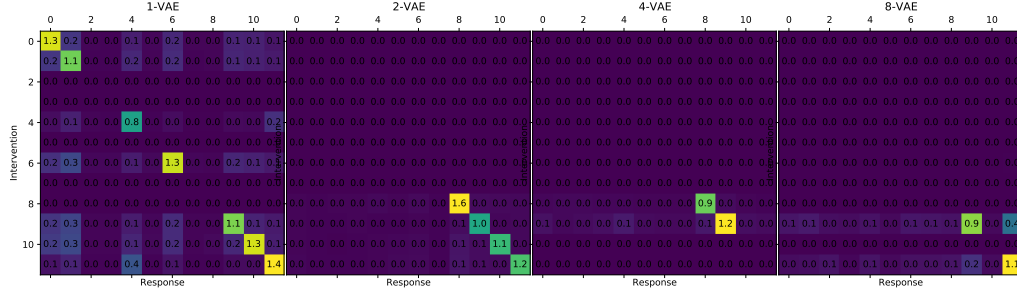


(b) Conditioned Response Matrices

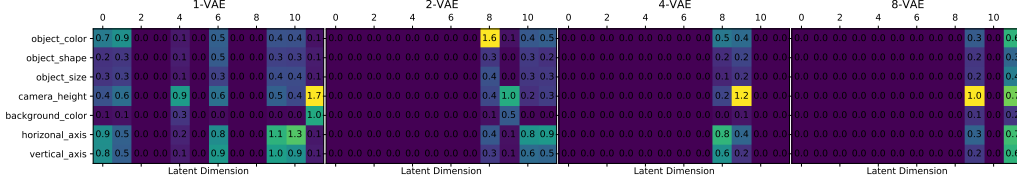


(c) DCI Responsibility Matrices

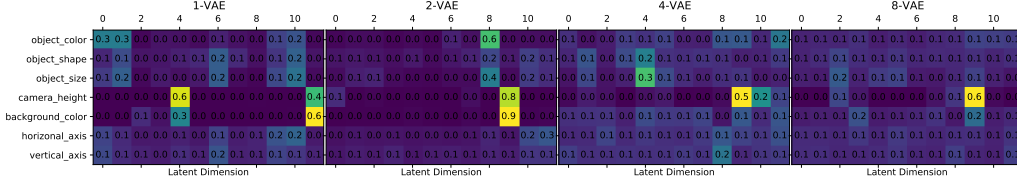
Figure 17: Response and Responsibility matrices for several VAEs ( $d = 12$ ) trained on the MPI3D Toy dataset.



(a) Latent Response Matrices



(b) Conditioned Response Matrices



(c) DCI Responsibility Matrices

Figure 18: Response and Responsibility matrices for several VAEs ( $d = 12$ ) trained on the MPI3D Real dataset.

Name	SS	CDS	DCI-D	IRS	MIG
1-VAE	7.81	0.69	0.33	0.58	0.32
2-VAE	17.66	0.86	0.17	0.59	0.14
4-VAE	17.38	0.66	0.11	0.61	0.05
8-VAE	23.63	1	0.13	0.79	0.1
1-VAE	4.36	0.61	0.24	0.51	0.07
2-VAE	10.13	0.69	0.26	0.72	0.24
4-VAE	17.5	0.4	0.09	0.75	0.04
8-VAE	17.85	0.7	0.08	0.71	0.04

Table 3: Structure Score ( $SS \times 100$ ) and disentanglement scores for the MPI3D Toy (first four rows) and Real (last four rows). Note that the substantial posterior collapse experienced by the VAEs with larger  $\beta$  values dramatically increases their structure scores, and somewhat improves the Causal Disentanglement Scores. While this may be misleading as it suggests those representations are more desirable, the significant posterior collapse is easy to spot using the Latent Response Matrices (figure 17b and 18a), underscoring the need for deeper analysis of learned representations rather than relying on a handful of scalar metrics.

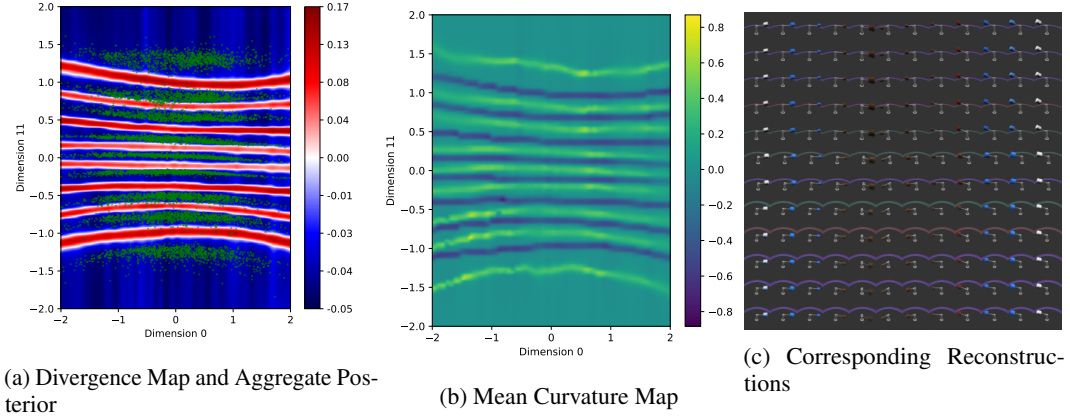


Figure 19: Visualization of the representation learned by the 1-VAE trained on MPI3D Toy.

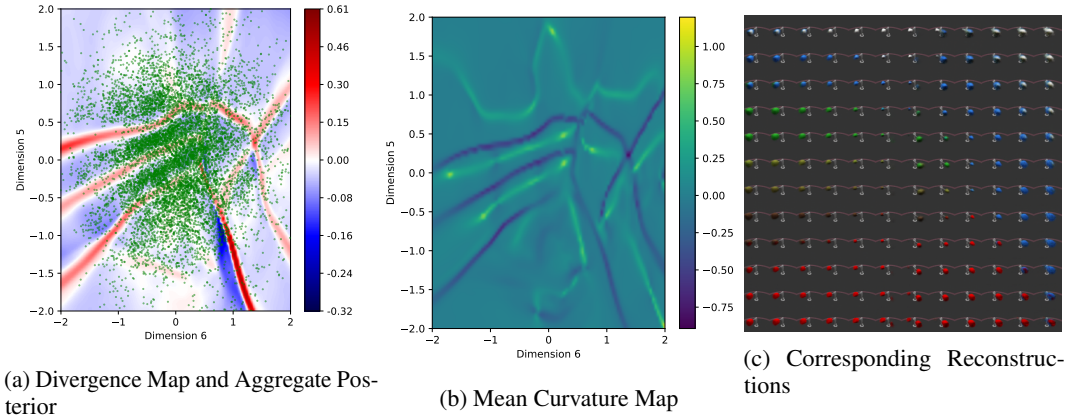


Figure 20: Visualization of the representation learned by the 1-VAE trained on MPI3D Toy.

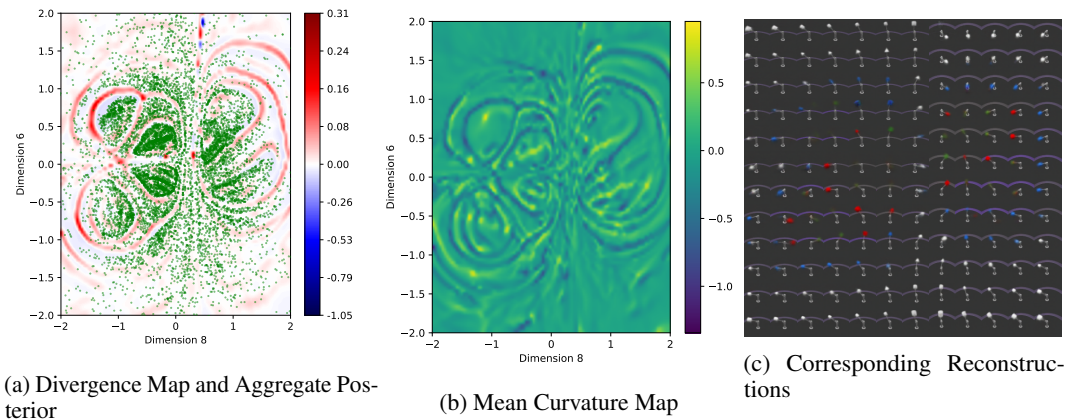


Figure 21: Visualization of the representation learned by the 4-VAE trained on MPI3D Toy. Note that due to posterior collapse, the full latent manifold is contained in this projection (see the corresponding response matrix in figure 17).

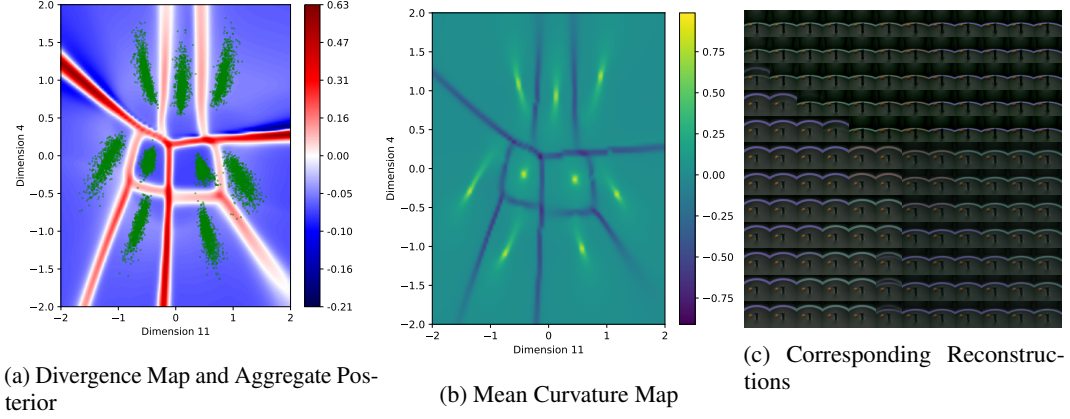


Figure 22: Visualization of the representation learned by the 1-VAE trained on MPI3D Real.

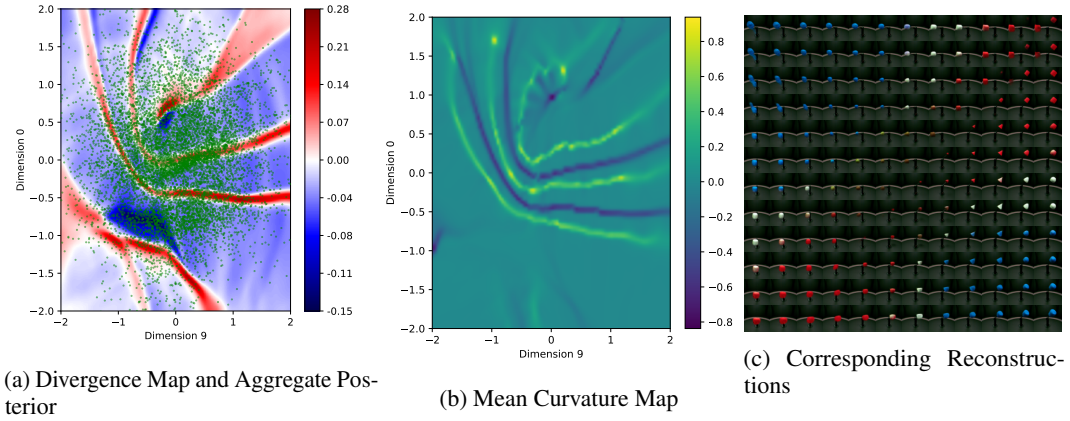


Figure 23: Visualization of the representation learned by the 1-VAE trained on MPI3D Real.

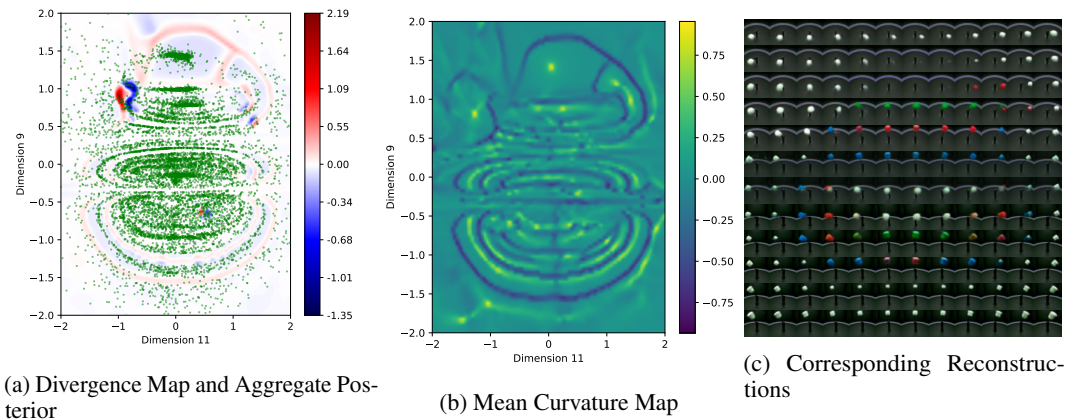


Figure 24: Visualization of the representation learned by the 8-VAE trained on MPI3D Real. Note that due to posterior collapse, the full latent manifold is contained in this projection (see the corresponding response matrix in figure 18).

### B.3 MNIST

Due to the computational cost of evaluating the response function over a dense grid, we focus our visualizations to 2D projections of the latent space. However, for MNIST and Fashion-MNIST, we train several VAE models to embed the whole representation into two dimensions  $d = 2$ , so that we can visualize the full representation. While the resulting divergence and curvature maps do not demonstrate as intuitive structure as in the disentangled representations for 3D-Shapes or MPI-3D, we can nevertheless appreciate the learned manifold beyond qualitatively observing reconstructions.





### B.3.1 MNIST

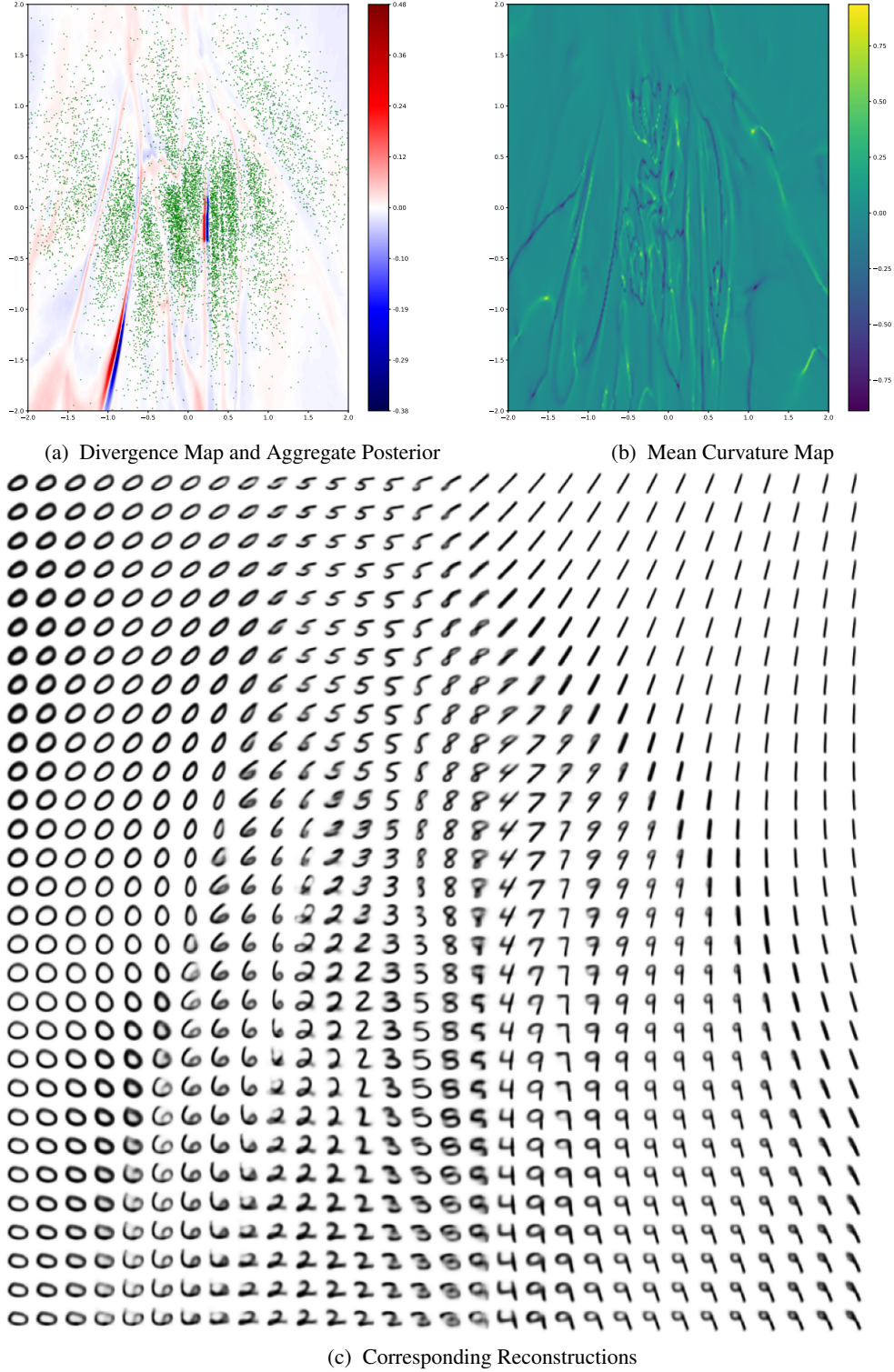


Figure 25: The full latent space for a VAE ( $d = 2$ ) model trained on MNIST. 25a shows the computed divergence of the response field in blue and red while the green points are samples from the aggregate posterior. 25b shows the resulting mean curvature, which identifies 10 points where the curvature spikes and the boundaries between the regions corresponding to different clusters in the posterior. Finally 25c shows the reconstructions over the same region. Note how the high divergence (red) regions correspond to boundaries between significantly different samples (such as changing digit value or stroke thickness).

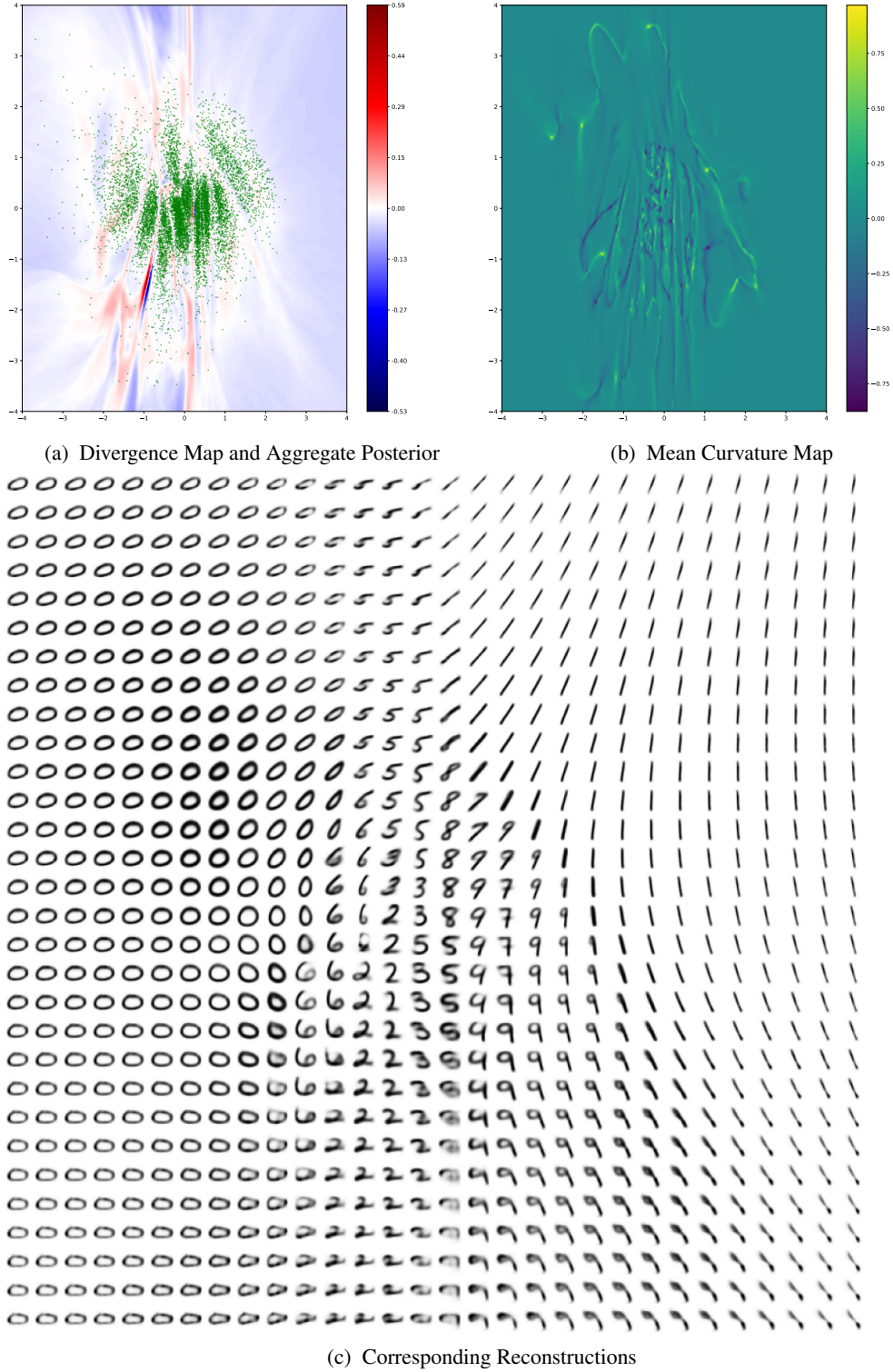
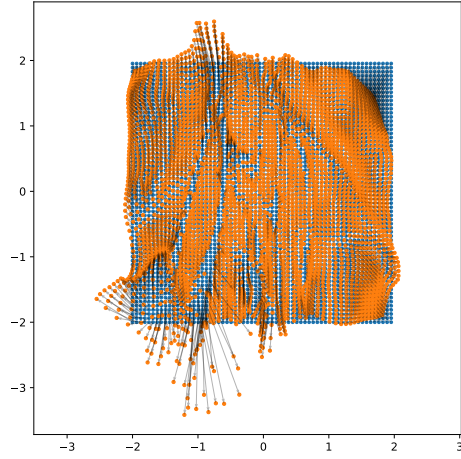
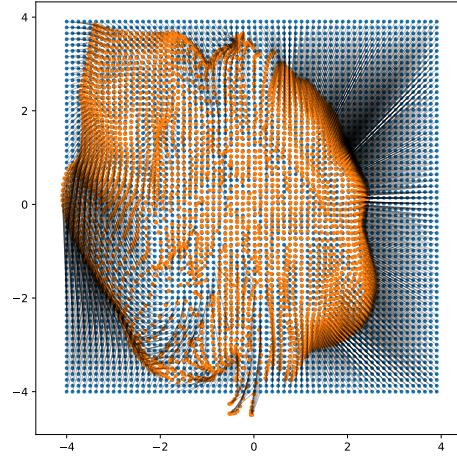


Figure 26: Same plot and model as figure 25, except over a larger range of the latent space  $[-4, 4]$ . Note that even though the posterior (green dots) is concentrated near the prior (standard normal), reconstructions far away (along the edges of the figure) still look recognizable, demonstrating the exceptional robustness of VAEs to project unexpected latent vectors back onto the learned manifold.





(a) Response field  $[-2, 2]$



(b) Response field  $[-4, 4]$

Figure 27: Response fields for the same model analyzed in figures 25 and 26. The blue dots show the initial latent samples, and the orange dots connected by the black arrows show the corresponding responses (the latent sample after decoding and reencoding).



### B.3.2 Fashion-MNIST

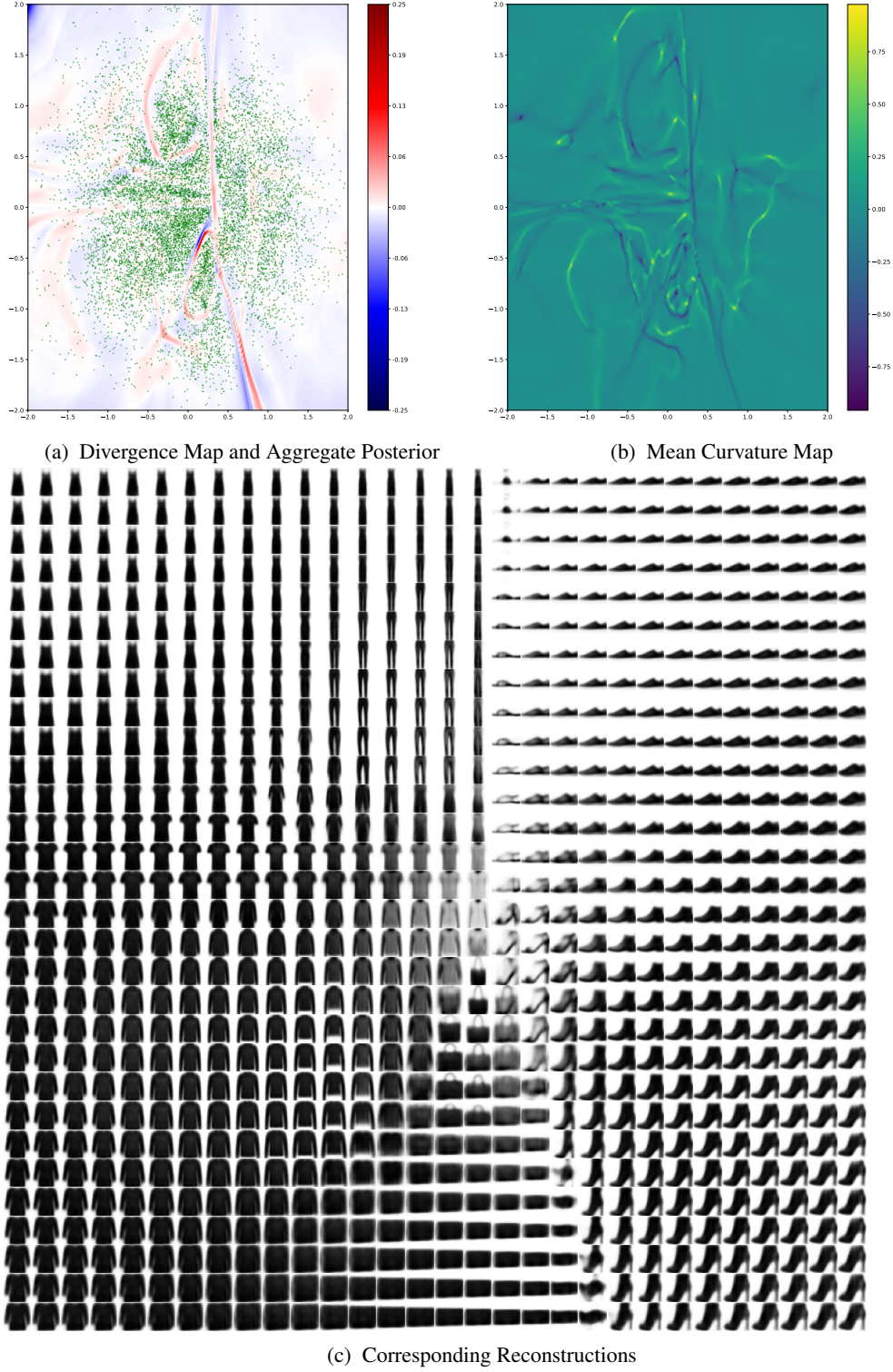
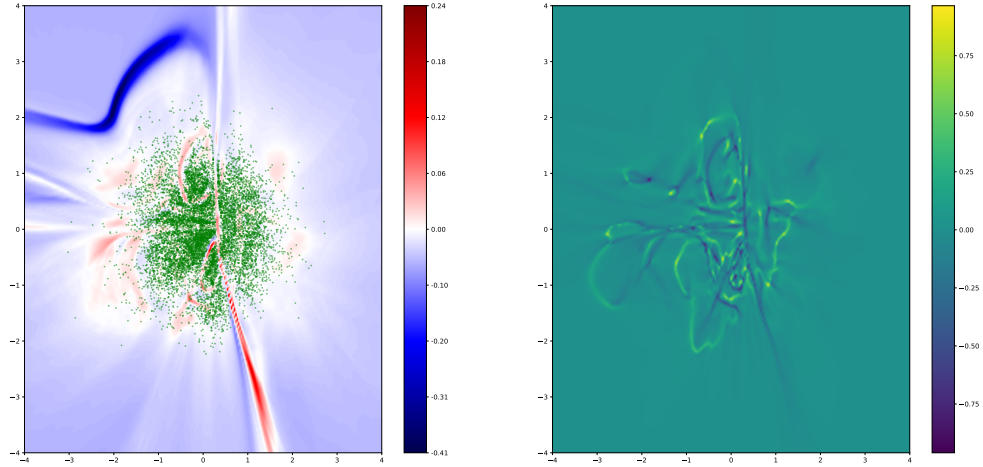
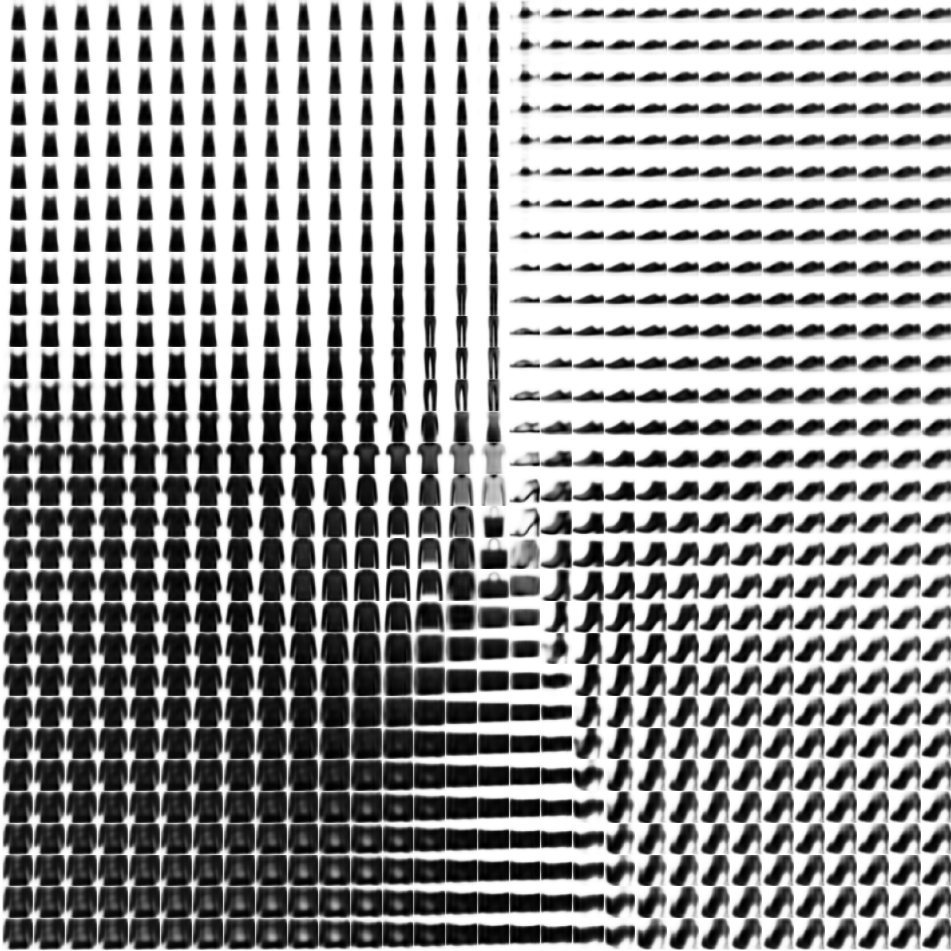


Figure 28: The full latent space for a 8-VAE ( $d = 2$ ) model trained on MNIST. 28a shows the computed divergence of the response field in blue and red while the green points are samples from the aggregate posterior. 28b shows the resulting mean curvature, which identifies 10 points where the curvature spikes and the boundaries between the regions corresponding to different clusters in the posterior. Finally 28c shows the reconstructions over the same region. Note how the high divergence (red) regions correspond to boundaries between significantly different samples (such as changing digit value or stroke thickness).



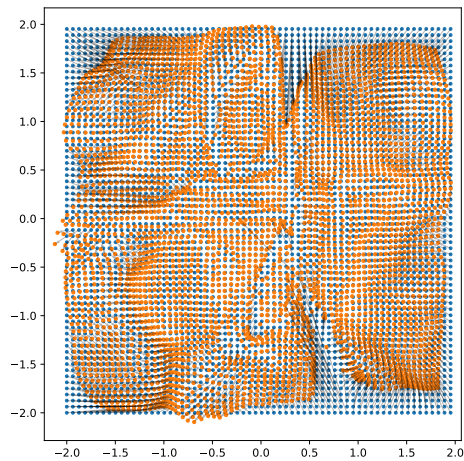
(a) Divergence Map and Aggregate Posterior

(b) Mean Curvature Map

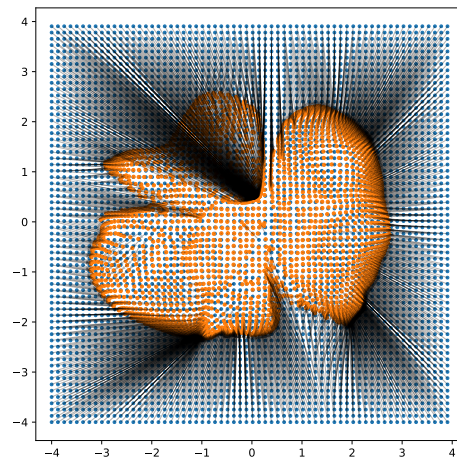


(c) Corresponding Reconstructions

Figure 29: Same plot and model as figure 28, except over a larger range of the latent space  $[-4, 4]$ . Note that even though the posterior (green dots) is concentrated near the prior (standard normal), reconstructions far away (along the edges of the figure) still look recognizable, demonstrating the exceptional robustness of VAEs to project unexpected latent vectors back onto the learned manifold.



(a) Response field  $[-2, 2]$



(b) Response field  $[-4, 4]$

Figure 30: Response fields for the same model analyzed in figures 28 and 29. The blue dots show the initial latent samples, and the orange dots connected by the black arrows show the corresponding responses (the latent sample after decoding and reencoding).